High Resolution Map of Interstellar Dust and Light Extinction in Our Galaxy Derived from Far-Infrared Intensities

Tsunehito Kohyama

A dissertation for the degree of Doctor of Philosophy

Department of Earth and School, Graduate School of Science, Osaka University, 1-1, Machikaneyama-cho, Toyonaka, Osaka 560-0043, Japan.

February, 2012

Abstract

The present study establishes a new method to derive the degree of the light extinction by the interstellar dust within the Galaxy. The method of present study is based on the far-infrared intensities at 60, 100, & 140 μm. A new Galactic extinction map is derived by the present study. This map will be used to estimate the degree of light extinction by the interstellar dust.

The method of the present study has a clear advantage over the standard method established by Schlegel, Finkbeiner, and Davis because the spatial resolution is 10 times higher than that of Schlegel et al. The interstellar dust that is in equilibrium with the interstellar radiation field radiates thermal emission in the far-infrared wavelengths longer than 100 μm. The dust column density (i.e., optical depth) can be derived from the observed intensities of the interstellar dust at longer than 100 μm. The present study derives the 140 μm intensity from the observed intensities at 60 & 100 μm. The 140 μm intensity map is derived with a 5′ spatial resolution in half of the sky. The present study derived the extinction with a higher spatial resolution than that of Schlegel et al. The difference of the extinction between the present study's map and Schlegel et al's map is significant in the galactic plane. In high galactic latitudes, on the other hand, the difference between the present study's map and Schlegel et al's map is not so large as much as in the galactic plane because the dust distribution is more uniform than that in the galactic plane.

Several previous studies derived the extinction on the basis of star catalogs at the visible to near-infrared wavelengths. These methods derive the extinction from the decrease of the observed star density or from the reddening of observed stars in a solid angle. The present study can detect much higher extinction than

that detected by these methods because the interstellar space in the visible to near-infrared wavelengths region is more optically thick than that in the far-infrared wavelengths. Fundamentally, these methods can not detect the interstellar dust behind the stars. These methods are not effective where the extinction is negligibly small because of low signal-to-noise ratios.

Acknowledgments

The author is very grateful to all the people who have contributed directly and indirectly to this thesis.

The author would like to thank Professor Dr. Hiroshi Shibai for his continuous support and encouragement in the author's study. The thesis could not have been accomplished without his support. His insight on the physics is free from any bias. His insight taught the author both how to conduct research. The author's work on the development of the *Far-Infrared Interferometry Experiment* (*FITE*) is also supported by him.

The author would like to thank Dr. Yasunori Hibi for his careful comments on this study. This study was based on his previous study on the far-infrared astronomy. The author would also like to Assistant Professor Dr. Misato Fukagawa, Associate Professor Dr. Takahiro Sumi, & Associate Professor Dr. Mitsunobu Kawada for their helpful comments on this study. These comments help the author to improve his manuscripts.

The author would like to express his gratitude to past and present members of both the *Infrared Astronomy Laboratory* of Osaka University and the *U-lab*. of Nagoya University. Their dedicated behavior on their studies and works has motivated the author to conduct his research.

This study was supported by Grant-in-Aid for challenging Exploratory Research (22654023).

Contents

List of Figures

List of Tables

Chapter 1

Introduction

Radiations from both extragalactic objects and inner-galactic objects are generally reduced and attenuated by the Galactic interstellar dust. The interstellar dust is a submicron size grain. As a result of the light scattering and absorption by the interstellar dust, the light extinction appears in a line of sight. The light extinction degree must be estimated in order to derive the correct flux of stellar objects.

The light extinction by the interstellar dust was firstly inferred by Trumpler (1930) through the reddening of starlight. The degree of the light extinction (i.e., A_λ) at a wavelength λ is defined as a ratio of flux density (i.e., F_ν) at wavelength λ between observed flux over an intrinsic flux. The degree of the light extinction A_λ is shown in common logarithm scale as

$$A_\lambda = -2.5 \log_{10} \left(\frac{F_{\nu,\text{observed}}}{F_{\nu,\text{intrinsic}}} \right), \tag{1.1}$$

where $F_{\nu,\text{ observed}}$ is an observed flux density at wavelength λ, and $F_{\nu,\text{ intrinsic}}$ is an intrinsic flux density that is not extinct. Equation (1.1) means that if an observed flux decreases by 100 times smaller, the extinction increases as much as 5 magnitudes. If the value of A_λ is revealed, $F_{\nu,\text{ intrinsic}}$ can be estimated correctly. A certain degree of light extinction by the interstellar dust introduces a redder star color because extinction at longer wavelength is smaller than that at a shorter wavelength. This reddening is defined as the color difference between the

intrinsic star spectrum and the observed star spectrum. An intrinsic star spectrum type can be predicted by a spectroscopic observation. By comparing intrinsic spectrum and observed spectrum, degree of the reddening of starlight can be estimated. The reddening index of E ($B-V$) is defined between 0.44 (B) μm and 0.55 (V) μm as

$$E(B-V)=\left(m_{B,\text{observed}}-m_{V,\text{observed}}\right)-\left(m_{B,\text{intrinsic}}-m_{V,\text{intrinsic}}\right), \tag{1.2}$$

where m_B and m_V is the apparent magnitude, which is defined as below

$$m_\lambda = -2.5\log_{10}\left(\frac{F_\nu}{F_{\nu,\text{threshold}}}\right), \tag{1.3}$$

where $F_{\nu,\text{ threshold}}$ is a threshold flux[1]. With Equation (1.1) and (1.3), Equation (1.2) is written by

$$E(B-V)=A_B-A_V. \tag{1.4}$$

E ($B-V$) is considered to be proportional to A_V because A_B is considered to be proportional to A_V. Then the extinction and reddening index is written by

$$A_V = R_V\left[E(B-V)\right]. \tag{1.5}$$

R_V is the proportional constant and can be estimated by the spectroscopic observation together with the assumption that the dust extinction goes to zero at very long wavelength. Generally R_V is 3.1 (e.g., Jones, West, & Foster 2011). If both the star luminosity and the distance to the star are measured, the extinction can be estimated by Equation (1.1). The star luminosity can be determined by the spectroscopic observation. In contrast, the distance measurement is difficult toward the extinction region. Therefore, usually the extinction is estimated by the reddening (Equation 1.4). But the other method is essential in order to estimate the light extinction toward extragalactic objects (e.g., galaxies) because the Galactic interstellar dust exists actually behind the Galactic stars.

The interstellar dust absorbs the interstellar radiation from stars and reradiates the thermal emission in the infrared wavelengths. *The Infrared Astronomy Satellite* (*IRAS*), which was launched in 1983 and observed 96% of the sky in the infrared at 4 wavelengths (12, 25, 60, & 100 μm), revealed that the interstellar dust covered the all-sky for the first time (*IRAS* Explanatory Supplement 1988) with a 5′ spatial resolution. Figure 1.1 shows the all-sky maps of the diffuse infrared intensities observed by *IRAS* at 60 and 100 μm.

[1] $F_{\nu,\text{ threshold}}$ is usually represented by the flux of VEGA, which is the brightest star in the constellation Lyra.

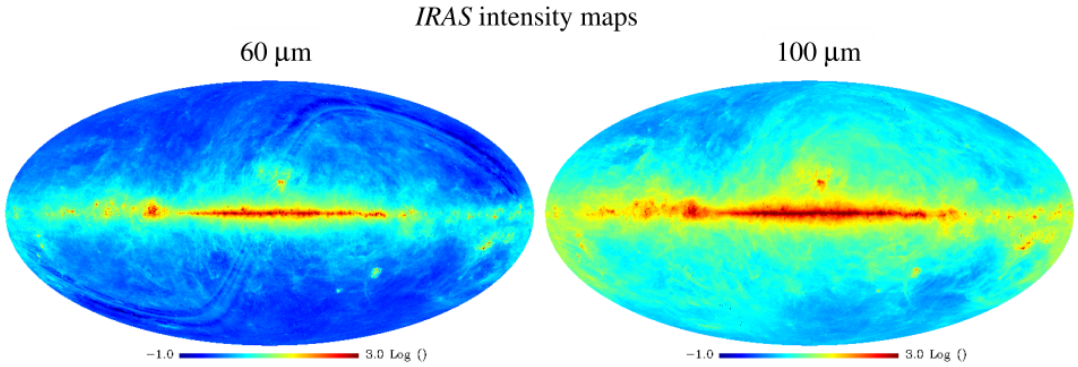

Figure 1.1: Results of the *IRAS* all-sky survey for the diffuse intensities at 60 and 100 μm with common logarithm scale. The range is 0.1 to 10^3 MJysr^{-1}. The distribution is shown in the Mollweide projection with the galactic coordinate. The interplanetary dust emission is subtracted by a standard model (Kelsall et al. 1998). The stripe feature in 60 μm image shows an uncertainty of the subtraction of the interplanetary dust emission. The 4% of the sky which *IRAS* did not observe are represented by the DIRBE data shown in Figure 1.2. The images are The Improved Reprocessing of the *IRAS* Survey (IRIS; Miville-Deschênes & Lagache 2005).

This *IRAS* results indicated that the radiation from extragalactic objects was extinct by the dust in "every line of sights". The Diffuse infrared Background Experiment (DIRBE) on the *Cosmic Background Explorer* (*COBE*) satellite, which was launched in 1989, observed the infrared all-sky at 10 wavelengths (1.25, 2.2, 3.5, 4.9, 12, 25, 60, 100, 140, & 240 μm) with a 0˚.7 spatial resolution (DIRBE Explanatory Supplement 1998). Figure 1.2 shows the all-sky maps of the diffuse infrared intensities observed by DIRBE at 60, 100, 140, and 240 μm. The emission from the interplanetary dust (IPD), which locates within the Solar system, was predicted by the DIRBE annual near-infrared observation (Kelsall et al. 1998). DIRBE observations correctly estimated the diffuse infrared intensity with a careful calibration method[2]. The result of the DIRBE observation revealed that the calibration of *IRAS* intensities was overestimated and must be corrected by the DIRBE calibration (Wheelock et al. 1994; Miville-Deschênes & Lagache 2005).

[2] Hauser et al. (1998) estimated the Cosmic Infrared Background (CIB) radiation on the basis of the DIRBE results for the first time.

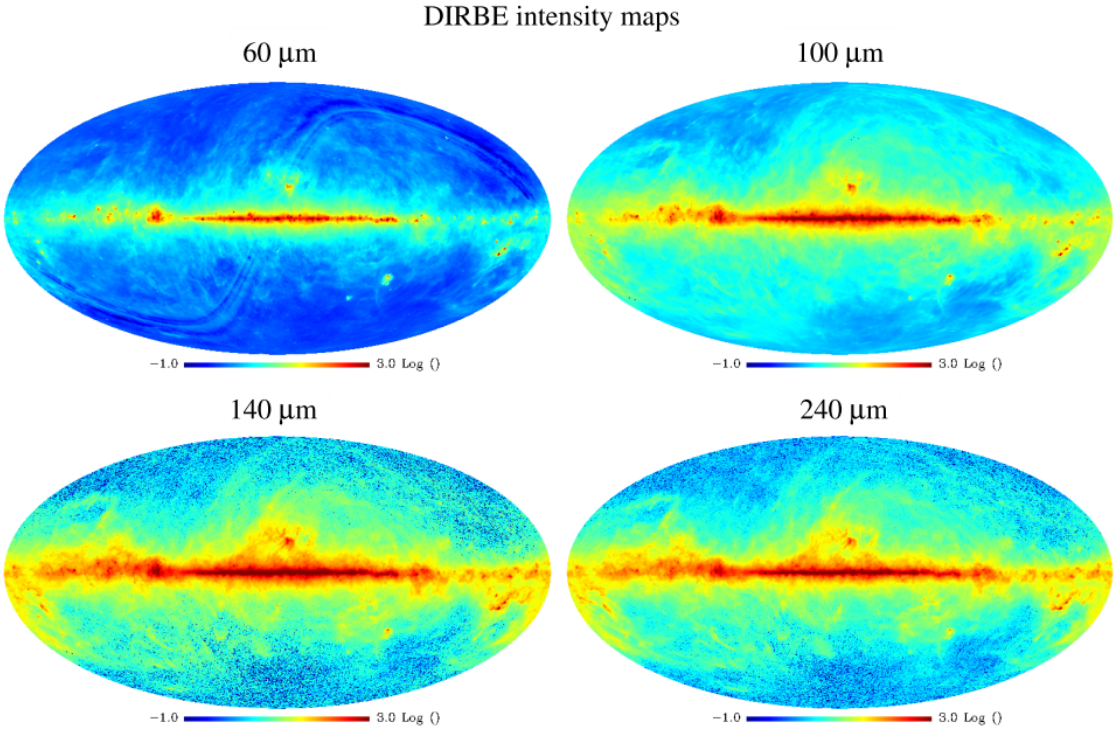

Figure 1.2: Results of the DIRBE all-sky survey for the diffuse intensities at 60, 100, 140, and 240 μm with common logarithm scale. The range is 0.1 to 10^3 MJysr^{-1}. The distribution is shown in the Mollweide projection with the galactic coordinate. The interplanetary dust emission is subtracted by a standard model (Kelsall et al. 1998). The stripe feature in 60 μm image shows an uncertainty of the subtraction of the interplanetary dust emission. Low signal-to-noise ratios in high galactic latitudes are apparent in 140 and 240 μm images. The images are The Zodi Subtracted Mission Average data (ZSMA; DIRBE Explanatory Supplement 1998).

The light extinction by dust is high in the ultraviolet (UV)–optical wavelength region, the observed data at these wavelengths must be corrected for the Galactic extinction along each line of sight. For example, statistical analyses of extragalaxies using the Sloan Digital Sky Survey (SDSS; York et al. 2000), which has a goal[3] with obtaining CCD imaging in the optical five broad bands over 10,000 deg^2 of high-latitude sky, require an accurate extinction map. For this purpose, Schlegel, Finkbeiner, & Davis (1998, hereafter SFD) have made an all-sky map of the Galactic extinction by using the all-sky far-infrared maps of

[3] SDSS has goals with the goals of obtaining CCD imaging in five broad bands (0.35, 0.48, 0.62, 0.77, and 0.92 μm) over 10,000 deg^2 of high-latitude sky, and spectroscopy of a million galaxies and 100,000 quasars over this same region. These goals have been realized in its seventh public data release (Abazajian et al. 2009).

IRAS and DIRBE. Figure 1.3 shows the SFD's extinction map, assuming R_V = 3.1. SFD's method depended upon the fact that the dust radiates infrared emission and is generally optically thin at the far-infrared wavelengths. SFD used the *IRAS* data at 100 μm as the observed dust emission and the DIRBE data at 100 and 240 μm to derive the dust temperature. The Galactic dust detected by DIRBE spanned a color temperature range of 17 to 21 K for an assumed the spectral emissivity index of 2 (Reach et al. 1995).

SFD assumed a single color temperature in each line of sight (i.e., one-zone model). SFD combined the observed dust intensity and the dust temperature in order to derive the dust column density. It was because that the observed dust emission was correlated with both the dust temperature and the column density. They found that their map reproduced intrinsic colors of elliptical galaxies, as estimated from the MgII index (Faber et al. 1989), with an accuracy of 16% which is roughly factor 2 improvement over the extinction map provided by Burstein & Heiles (1978, 1982) based on HI 21-cm emission. This accuracy means that "the one-zone model" was reasonable.

Despite the SFD's efforts, their extinction map may not trace small-scale variation because the dust temperature resolution limited by DIRBE (Arce & Goodman 1999). Figure 1.4 shows that the spatial resolution difference is significant between the *IRAS* and DIRBE intensity map at 100 μm. As described below, the dust temperature was not derived correctly by the *IRAS* data only. To derive the dust temperature and column density, the dust size is important; the dust size is classified into three groups (e.g., Désert, Boulanger, & Puget 1990): polycyclic aromatic hydrocarbon (PAH), very small grain (VSG), and large grain (LG). LG absorbs UV–optical photons and reradiates the absorbed energy in far-infrared. The observed far-infrared intensity at longer than 100 μm is dominated by LGs (e.g., Sodroski et al. 1997). LGs are considered to be in equilibrium with the interstellar radiation field (e.g., Draine & Anderson 1985) radiate thermal emission with an equilibrium temperature. Therefore, assuming a spectral emissivity index, the dust temperature and the optical thickness can be derived from the far-infrared spectral energy distribution (SED). The dust extinction in the UV and optical wavelength regions can be derived from the far-infrared SED if the dust optical depth of LG is proportional to the extinction of each grain component (PAH+VSG+LG).

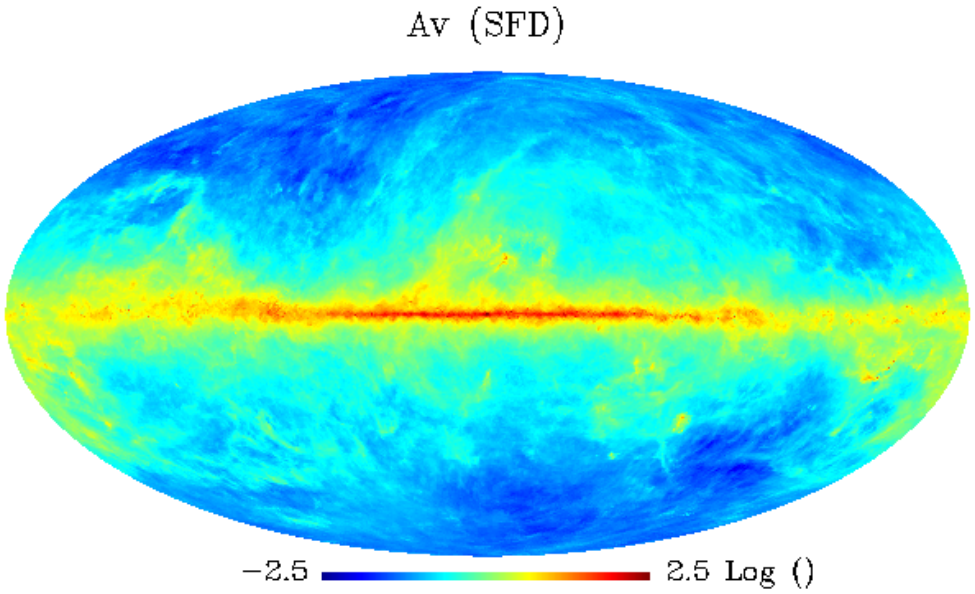

Figure 1.3: All-sky extinction map at V band derived by SFD with common logarithm scale. Range is 0.003 to 300 mag. R_V = 3.1 is assumed. The distribution is shown in the Mollweide projection with the galactic coordinate.

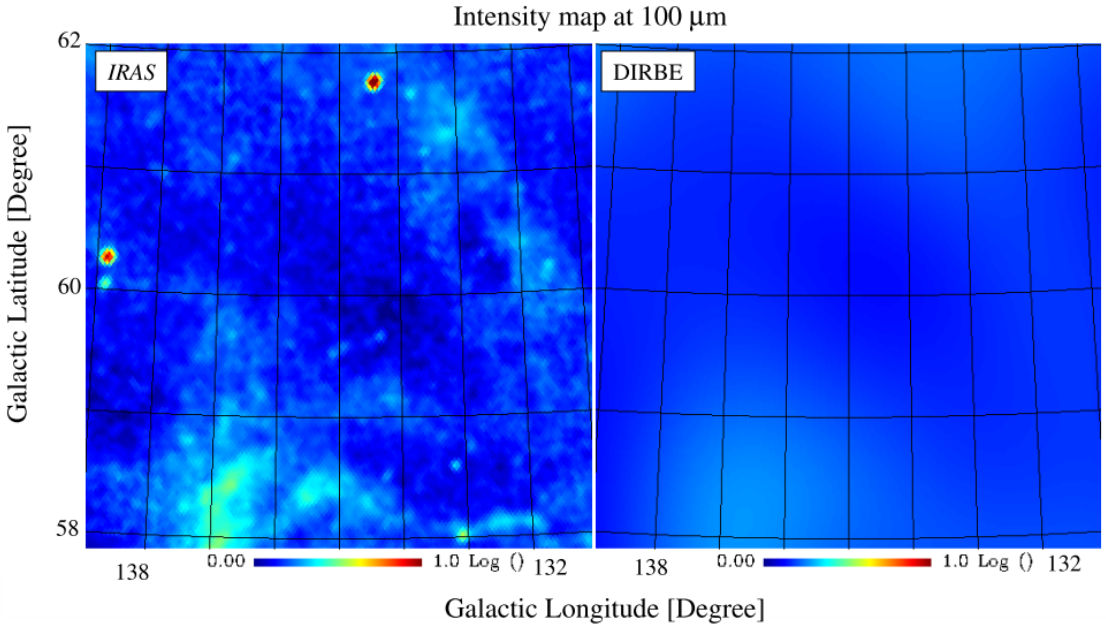

Figure 1.4: Intensity maps of *IRAS* and DIRBE at 100 µm with common logarithm scale. Range is 1 to 10 MJysr^{-1}. Spatial resolution difference is significant. Spatial resolutions of *IRAS* and DIRBE are 5′ and 0°.7, respectively. The distribution is shown in the Gnomonic projection with the galactic coordinate.

PAH and VSG, in contrast to LG, are stochastically heated by a single photon to high temperatures and cooled by radiation shorter than 60 μm (Greenberg 1968; Aannestad & Kenyon 1979; Draine and Anderson 1985). As a significant fraction of the 60 μm intensity usually comes from VSGs (Désert, Boulanger, & Puget 1990), the LG temperature cannot be derived from the *IRAS* 60 and 100 μm band data only.

Several extinction maps have been derived on the basis of star catalogs. Dobashi et al. (2005) derived a visual extinction map within $|b| < 40^\circ$ with a 6′ spatial resolution (Figure 1.5) using the optical database Digitized Sky Survey I (DSS), which comprises a set of all-sky photographic surveys at 0.44 (*B*), 0.55 (*V*), and 0.66 (*R*) μm conducted with the Palomar and UK Schmidt telescopes (Lasker 1994). Dobashi et al. (2005) derived the extinction on the basis of the star counting method (Wolf 1923), which is a classical method to estimate the extinction distribution. Star counting method measures the change of star density per solid angle. Star density in a direction with a certain degree of extinction tends to be smaller than that in a direction with negligible extinction. The Dobashi's map was based on the 7 hundred million stars. Their map was the first large extinction map on the basis of the star counting method. They found 2448 dark cloud, which is a dense region composed from the interstellar dust and is considered to be correlated with the star formation. Since the star counting technique cannot measure the dust behind the stars, its accuracy can worsen in directions where the extinction is high, depending on many parameters such as the angular density of stars, their location from the molecular cloud, and the distribution of the distances of the dust. Therefore, this technique may be ineffective for the correction of the Galactic extinction toward extragalactic objects near the Galactic plane.

In order to found dark clouds more dense than that Dobashi (2005) found, Dobashi (2011) derived an all-sky extinction map with a 1′–12′ spatial resolution (Figure 1.6) using the Two Micron All Sky Survey Point Source Catalog (2MASS PSC), set of all-sky photographic surveys at the 1.25 (*J*), 1.65 (*H*), and 2.17 (*Ks*) μm conducted with the 1.3 m telescope at Mt. Hopkins and CTIO (Skrutskie et al. 2006). Dobashi (2011) derived the color excess of a star by using the "X percentile method," a new extension of the Near Infrared Color Excess method (NICE; Lada et al. 1994; Rowels and Froebrich 2009). Compared with the NICE method, the X percentile method is more robust against contamination by foreground stars because it statistically corrects for the

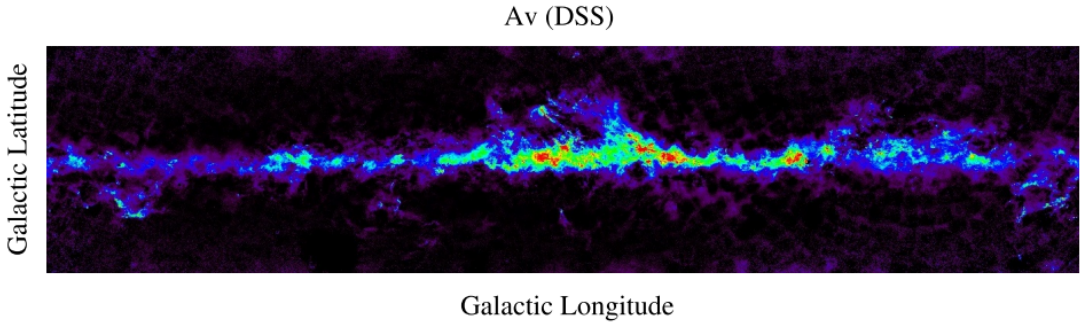

Figure 1.5: The extinction map at V band on the basis of the star counting method by Dobashi et al. (2005) with linear scale. Range is 0 to 5 mag. The map was derived within $|b| < 40^{\circ}$. The boundaries of DSS photographic plates are apparent. The distribution is shown in the Cartesian projection with the galactic coordinate.

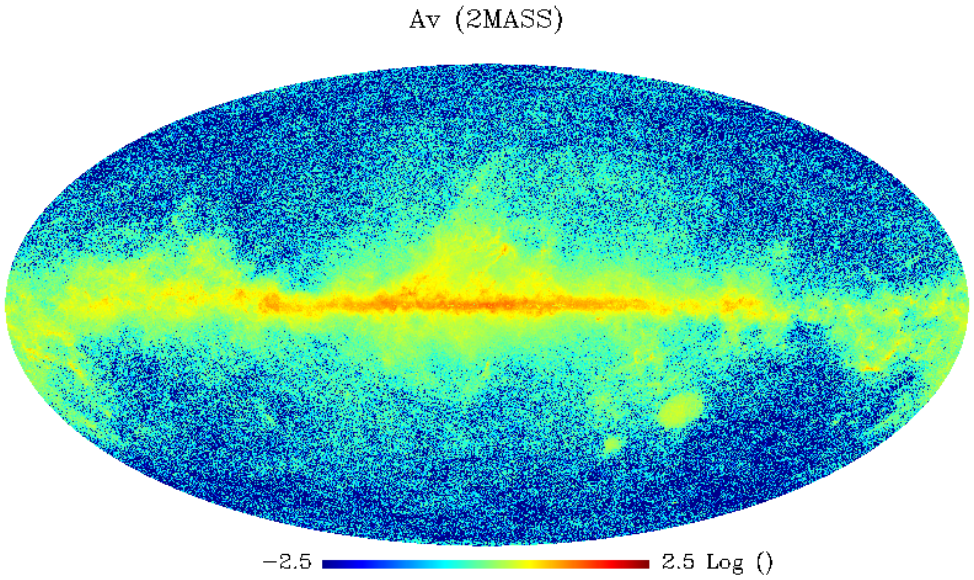

Figure 1.6: The extinction map at V band on the basis of the 2MASS Point Source Catalog (Dobashi 2011) with common logarithm scale. Range is 0.003 to 300 mag. Low signal-to-noise ratio in high galactic latitudes is apparent. The distribution is shown in the Mollweide projection with the galactic coordinate.

effects of stars in the foreground. They found 7614 dark clouds. K. Dobashi renewed the estimation[4] of the background star colors using a star catalog simulated by Robin et al. (2003). This method measures the dust only in front of the stars and is based on the near-infrared radiation. Therefore, the precision of this method can degrade in directions of high extinction. In addition, the signal-to-noise (S/N) ratio can decrease in directions of small extinction such as that in high galactic latitudes. Therefore, their technique may be ineffective for the correction of galactic extinction toward extragalactic.

To improve the reddening of the extragalactic object, the author assumed the color–color correlations between 60, 100, and 140 μm that were found by Hibi et al. (2006). They analyzed Zodi-Subtracted Mission Average (ZSMA) data of the Galactic plane within $|b| < 5^{\circ}$, Large Magellanic Cloud (LMC), and Small Magellanic Cloud (SMC). They identified two groups having very tight correlations in the color-color diagram. These correlations are not produced with the model by Li & Draine (2002). Bot et al. (2009) also argued that the model by Draine & Li (2007) does not explain the Multiband Imaging Photometer for *Spitzer* satellite (MIPS) and *IRAS* data. By using Hibi et al.'s (2006) correlation, the dust temperature and the dust extinction can be obtained with 5′ resolution only from the *IRAS* data.

[4] http://darkclouds.u-gakugei.ac.jp/2MASS/download.html

Chapter 2

Analysis and Data for Far-Infrared Intensity

In this chapter, analysis and data for the far-infrared intensities are described. In this study, the Galactic extinction by the interstellar dust is derived on the basis of the far-infrared data. Color-color correlations between the far-infrared intensities are analyzed with the DIRBE data. Intensity at 140 μm is derived by the *IRAS* data at 60 and 100 μm assuming the color-color correlations. This intensity at 140 μm and the *IRAS* intensity at 100 μm are combined to derive the dust temperature distribution with a 5′ spatial resolution.

2.1 Analysis

The intensity at 140 μm is derived from the intensities at 60 and 100 μm of the *IRAS* data by using the tight correlation between 60, 100, and 140 μm found by Hibi et al. (2006). To test this method, the author selected a sample area in the Cygnus region. The selected area is 80° to 90° in the Galactic longitudes and −4° to −8° in the Galactic latitude. The IPD emission and the cosmic infrared background emission possibly contaminate the Galactic diffuse emission (e.g., Sodroski et al. 1997). However, as the Cygnus region is located at 60° in the ecliptic latitude, the subtraction of the IPD component has only a minor contribution to the uncertainty about the derivation of extinction discussed later.

The cosmic infrared background emission is negligible, since the far-infrared intensity is high enough in the Cygnus region.

In general, the interstellar space in the Galaxy is optically thin in the far-infrared wavelength region. The far-infrared intensity is written by

$$I_\nu(\lambda) = \tau_{100\mu\mathrm{m}} \times \left(\frac{100\,\mu\mathrm{m}}{\lambda} \right)^{\beta} \times B_\nu(\lambda, T_d), \tag{2.1}$$

where $I_\nu(\lambda)$ is the intensity at wavelength λ, $\tau_{100\,\mu\mathrm{m}}$ is the optical depth at 100 μm, T_d is the dust temperature, and β is the spectral emissivity index. $B_\nu(\lambda, T_d)$ is the Planck function. A one-zone model is adopted, i.e., the dust temperature is assumed to be constant along each line of sight. As reported by SFD, one-zone model is reasonable. Spectral emissivity index of 2 is adopted according to the previous study (Drain & Lee 1984; Hibi et al. 2006; SFD) for comparison. Because the published DIRBE all-bands intensities were derived by assuming a source spectrum, νI_ν is constant, the color correction should be applied to the observed data with the photometric bands of DIRBE. The color correction factor $K_\lambda(\beta, T_d)$ is determined from the spectral emissivity index and the dust temperature, if the spectrum is written by Equation (2.1). The conversion from the observed (uncorrected) intensity to the color-corrected intensity is given by Equation (2.2) with the color correction factor

$$I_{\nu,c}(\lambda) = \frac{I_\nu(\lambda)}{K_\lambda(\beta, \mathrm{T_d})}, \tag{2.2}$$

where $I_{\nu,\mathrm{c}}(\lambda)$ represents the color-corrected intensity. The color-correction factor $K_\lambda(\beta, \mathrm{T_d})$ is determined from the spectral emissivity index and dust temperature, assuming the spectrum given by Equation (2.1). The color-correction factor is unique for each instrument, and those of the *IRAS* and DIRBE intensities are referred in the respective explanatory supplement. In this study, color corrections are applied for the intensities at 140 and 100 μm, but not for that at 60 μm as reported in previous studies (Hibi et al. 2006). This is because the SED shape around 60 μm cannot be described by Equation (2.1). Such correction affects the intensities by few percentage points, and hence is not crucial for the results by the present study.

Table 2.1: Summary of the far-infrared data

	Wavelength [μm]	Spatial resolution [arcmin]	1σ noise level [$MJysr^{-1}$]	Calibration error [%]	IPD emission model
IRAS	60	4′.0	0.03	10.5	Kelsall et al. (1998)
	100	4′.3	0.06	13.5	
DIRBE	60	42′	0.09	10.5	
	100		0.1	13.5	
	140		2.4	10.6	

2.2 Far-Infrared Data

The far-infrared data are summarized in Table 2.1. The images of ZSMA, which is used as the DIRBE image in this study, are available in the Quadrilateralized Spherical Cube (QSC) projection and the data are binned to 393,216 pixels with a 19′.5 pixel scale. The Improved Reprocessing of the *IRAS* Survey (IRIS) by Miville-Deschênes & Lagache (2005) was used as the *IRAS* image. The IRIS maps are IPD-subtracted ones, the strip patterns are eliminated with a 2-D Fourier filter, and the calibration is rescaled with the DIRBE absolute calibration. The IPD emission both in the IRIS and ZSMA images was already subtracted on the basis of the model of Kelsall et al. (1998).

Table 2.2 shows the notations for *IRAS* and DIRBE intensities at 60, 100, 140 μm in this paper. The *IRAS* intensity at 140 μm was derived in this paper.

Table 2.2: Notations for the *IRAS* and DIRBE data

Notation	Observation Instrument
IRAS60	intensity observed by *IRAS* at 60 μm. The IRIS image.
IRAS100	same as above, but at 100 μm
IRAS140	intensity derived in this work at 140 μm.
DIRBE60	intensity observed by DIRBE at 60 μm. Zodi-subtracted Mission Average
DIRBE100	same as above, but at 100 μm
DIRBE140	same as above, but at 140 μm

Chapter 3

A Galactic Extinction Map of the Cygnus Region

To test the validity of a new method of making a high-resolution dust extinction map, the Cygnus region has been analyzed. First, color-color correlations of the Cygnus region are identified. The correlations are similar with the previous results reported by Hibi et al. (2006). Intensity at 140 μm with a 5′ spatial resolution (i.e., IRAS140) is derived from IRAS60 and IRAS100. This IRAS140 and IRAS100 are combined to derive dust temperature distribution. This dust temperature and IRAS100 are combined to derive the optical depth at 100 μm. Then the extinction is derived. In this chapter, the results of the analysis and compare them with those of SFD and Dobashi et al. (2005) are reported. Content of this Chapter is published as Kohyama et al. The Astrophysical Journal, 719, 873, 2010.

3.1 Color-Color Correlations in the Cygnus Region

The color-color diagram was made from the DIRBE data in the Cygnus region using the same procedure as Hibi et al. (2006). Hibi et al. (2006) indicated that there were two tight correlations in the Galactic plane. The major group is called the main-correlation, and the minor group the sub-correlation. The main-correlation and the sub-correlation are fitted with Equations (3.1) and (3.2), respectively

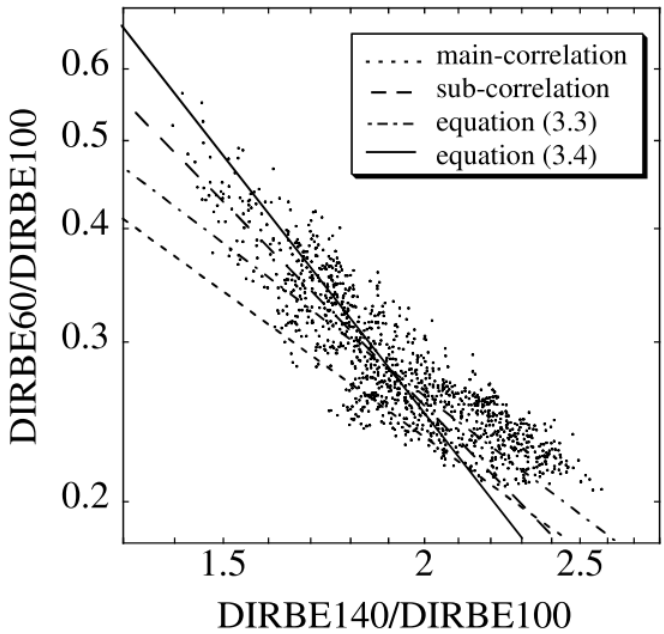

Figure 3.1: Color–color diagram between 60, 100, and 140 μm in the Cygnus region. The horizontal axis is the 140–100 μm color, while the vertical axis is the 60–100 μm color. The data points are from DIRBE. The main-correlation, the sub-correlation, Equation (3.3), and Equation (3.4) are represented by the doted line, dashed line, dash-dotted line, and solid line, respectively.

$$\frac{\mathrm{DIRBE140}}{\mathrm{DIRBE100}} = 0.65 \times \left(\frac{\mathrm{DIRBE60}}{\mathrm{DIRBE100}} \right)^{-0.78} . \tag{3.1}$$

$$\frac{\mathrm{DIRBE140}}{\mathrm{DIRBE100}} = 0.93 \times \left(\frac{\mathrm{DIRBE60}}{\mathrm{DIRBE100}} \right)^{-0.56} . \tag{3.2}$$

Hibi et al. (2006) and Hirashita et al. (2007) indicated that the main-correlation represents the lines of sight along which the ISRF is constant, and the sub-correlation represents the lines of sight along which the ISRF varies greatly.

The color-color diagram of the Cygnus region is shown in Figure 3.1. In contrast to the Galactic plane, the data points satisfying DIRBE60/DIRBE100 < 0.28 do not follow the main-correlation and other data points seem to follow the sub-correlation with a small offset. Therefore, the author tried to fit the data points in two regions divided at the DIRBE60/DIRBE100 ratio is 0.28. Least-squares fitting with two parameters of power and offset in the color-color diagram provided the following two relationships:

$$\frac{\mathrm{DIRBE140}}{\mathrm{DIRBE100}} = 0.73 \times \left(\frac{\mathrm{DIRBE60}}{\mathrm{DIRBE100}} \right)^{-0.75} . \quad (3.3)$$

$$\frac{\mathrm{DIRBE140}}{\mathrm{DIRBE100}} = 1.09 \times \left(\frac{\mathrm{DIRBE60}}{\mathrm{DIRBE100}} \right)^{-0.44} . \quad (3.4)$$

The coefficients of correlations of the former and latter cases are □0.7 and □0.8, respectively.

3.2 Galactic Extinction Map

IRAS140 was calculated from IRAS60 and IRAS100 for four cases listed in Table 3.1 in addition to the SFD method. At first, the author uses Equation (3.4) for all data points, and calls this the single case. As shown in Figure 3.1, this relation is similar to the sub-correlation, and approximately represents all the data points.

However, the scatter of the data points around the lines of Equations (3.3) and (3.4) does not reflect the photometric error included in the DIRBE's individual data points but actual variation. The photometric error was dominated by the electric noise. The noise level of DIRBE140 is 2.4 MJysr$^{\square 1}$ (DIRBE Explanatory Supplement 1998). Actually, the rms noise of DIRBE140 is 2 MJysr$^{\square 1}$ in the high latitude sky (b > 70˚). As the lowest intensity is 30 MJysr$^{\square 1}$ in the present analysis of the Cygnus region, the noise does not contribute to the scatter in Figure 3.1. The noise levels of DIRBE60 and DIRBE100 are negligible compared to the intensities at those bands. Therefore the scatter should be actual variation, and the fitting with a single line as above introduces an additional error into the estimation of temperature. Therefore, the author adopted the following method for the latter three cases as in Table 3.1. Each data point in Figure 3.1 was plotted from the DIRBE data with poor spatial resolution. SFD determined the dust temperature only from the DIRBE data, and thus, small-scale variation of the dust temperature was smeared out. On the other hand, we can use IRAS60 and IRAS100 with better spatial resolution, and we are aware of the reasonably good correlations. Therefore, the author initially plotted a single line with the same inclination as that of Equation (3.3) or (3.4) just at the data point plotted based on the DIRBE.

Table 3.1: Calculation Methods for SFD and Four New Cases

Notation	Method
A_V(SFD)	Schlegel, Finkbeiner, & Davis (1998)
A_V(single)	A single best-fit line, Equation (3.4)
A_V(shallow)	A line with the inclination of Equation (3.3) at each DIRBE data point
A_V(steep)	Same as A_V (shallow) but with the inclination of Equation (3.4)
A_V(best)	Combination of A_V (shallow) and A_V (steep) of Equation (3.6)

Next, the ratio of IRAS60 and IRAS100 is applied to the vertical axis of Figure 3.1 to determine the ratio of IRAS100 and IRAS140. Equation (3.5) indicates this method.

$$\frac{\text{IRAS140}}{\text{IRAS100}} = \frac{\text{DIRBE140}}{\text{DIRBE100}} \left(\frac{\text{DIRBE60}}{\text{DIRBE100}} \div \frac{\text{IRAS60}}{\text{IRAS100}} \right)^{b}. \tag{3.5}$$

The power index b is −0.75 or −0.44.

According to the correlation recognized in Figure 3.1, three cases are adopted as in Table 3.1: inclination of Equation (3.3), inclination of Equation (3.4), and a combination of both inclinations. The case of b = −0.75 is called as the shallow case and the case of b = −0.44 is called as the steep case. The last case is called the best-fit case that changes the power according to Equation (3.6) for better fitting;

$$b = \begin{cases} -0.75 & \left(\dfrac{\text{IRAS60}}{\text{IRAS100}} < 0.28 \right) \\ -0.44 & \left(\dfrac{\text{IRAS60}}{\text{IRAS100}} \geq 0.28 \right) \end{cases}. \tag{3.6}$$

This new method, corresponding to the latter three cases, is based on the fact that the scatter around a single fitted line may represent some actual variation and there may still remain a correlation with a similar inclination around each data point. It can be interpreted that SFD adopted a vertical line at each data point for the derivation of the temperature in Figure 3.1, whereas the latter three cases of the present study adopted a tilted line at each data point representing the actual correlation found by Hibi et al. (2006).

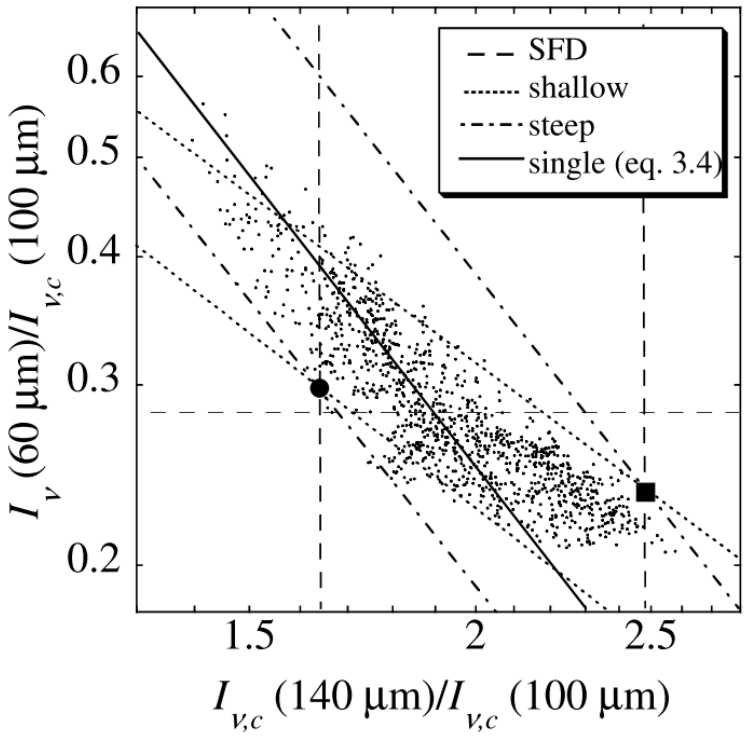

Figure 3.2: Explanation of A_V calculation on the color–color diagram between 60, 100, and 140 μm in the Cygnus region. The horizontal dashed line shows I_ν (60 μm)/$I_{\nu,c}$ (100 μm) = 0.28. The circle and square are points arbitrarily selected in regions of I_ν (60 μm)/$I_{\nu,c}$ (100 μm) > 0.28 and < 0.28, respectively.

The scatter from Equation (3.3) or (3.4) produces no error. The DIRBE data were regridded from 0˚.32 pixels to 5′ pixels, the same as those of *IRAS* with the sphere-approximation interpolation. As a result of this transformation, IRAS140 each pixel can be calculated using Equation (3.5).

Figure 3.2 shows the difference in the methods of calculating the dust temperature among five cases: SFD, single, shallow, steep, and best-fit. The best-fit is represented by the combination of the steep case and the shallow case at $I_{\nu,c}$ (60 μm)/$I_{\nu,c}$ (100 μm) = 0.28. The difference between the present method and SFD appears in the difference between the inclinations of lines. The deviation of IRAS60/IRAS100 = 0.28 from that of the DIRBE data is reflected for DIRBE140/DIRBE100 = 0.28 that corresponds to the dust temperature. Therefore, small-scale variation of the dust temperature should arise between the present method and SFD.

In the above mentioned method, IRAS140 was calculated from IRAS60 and IRAS100 with DIRBE data for the four cases. The dust temperature was

calculated from IRAS100 (i.e., observed 100 μm intensity) and IRAS140 derived by Equations (2.1). The *IRAS* data must be color-corrected as the DIRBE data. The color-correction factors were quoted from the *IRAS* Explanatory Supplement (Beichman et al. 1988). The color-corrected intensity at 140 μm is derived by the intensity at 60 μm and the color-corrected intensity at 100 μm. The optical depth at 100 μm is written as

$$\tau_{100\,\mu\mathrm{m}} = \frac{\mathrm{IRAS100}}{B_\nu(\lambda, T_d)}. \tag{3.7}$$

A_V is calculated by

$$A_V = 865.85 A_{100\,\mu\mathrm{m}}, \tag{3.8}$$

where $A_{100\,\mu\mathrm{m}} = 1.086\tau_{100\,\mu\mathrm{m}} = 2.5\times\log_{10}e\times\tau_{100\,\mu\mathrm{m}}$. The value of the conversion factor from $A_{100\,\mu\mathrm{m}}$ to A_V is quoted from Mathis (1990) assuming $R_V = 3.1$.

3.3 Result

A_V values in the Cygnus region are calculated for the four cases. Figure 3.3 shows the histogram of A_V (best) □ A_V (SFD). The standard deviation is 3.4. Figure 3.4 shows the histograms of A_V (best) □ A_V (shallow) and A_V (best) □ A_V (steep). The standard deviations are 1.2 and 0.83, respectively. Figure 3.5 shows the histogram of A_V (steep) □ A_V (single). The standard deviation is 1.9.

Figure 3.6 compares the dust temperature maps made by the best-fit case of the present study with those by SFD. The dust temperature distribution of the present study shows small-scale spatial variation that is not apparent in the map by SFD. The maximum and the standard deviation of the temperature difference between the two maps are 5 K and 0.5 K, respectively.

Figure 3.7 shows the A_V distribution of this area. The fluctuation of both the maps seems to have similar angular scales. However, the A_V values of both the maps differ from each other.

To analyze the reason for these differences, the differences in temperature and A_V are shown in Figure 3.8. The sign of the left panel of Figure 3.8 is reversed compared to that of the right panel so as to visually check the dependence because A_V has a negative dependence on temperature. It can be seen that the two maps resemble each other remarkably, which means that the difference in A_V originates from the difference in the derived temperature.

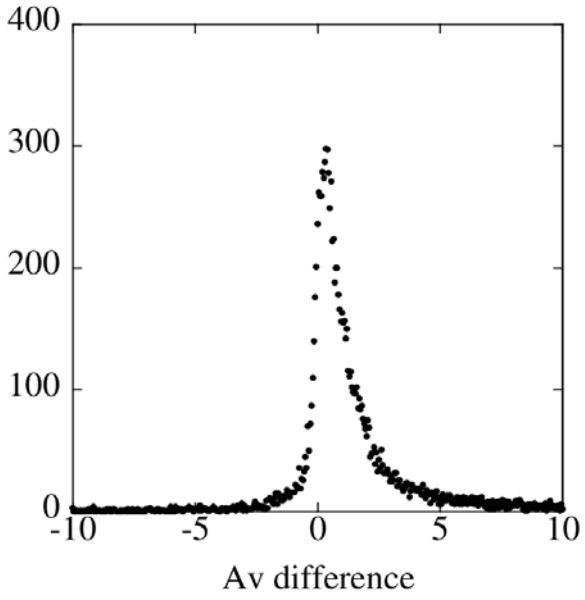

Figure 3.3: Histogram of the A_V difference of A_V (best) – A_V (SFD). Bin size is 0.05 mag.

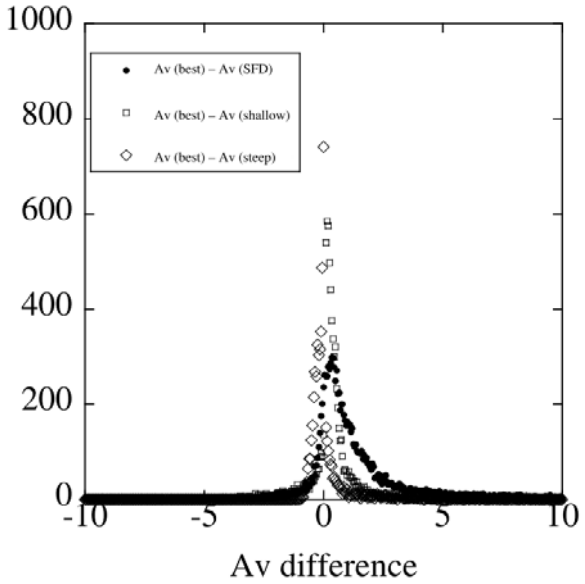

Figure 3.4: Histogram of the A_V differences in the Cygnus region. Bin size is 0.05 mag. Filled circles represent the same differences as in Figure 3.3.

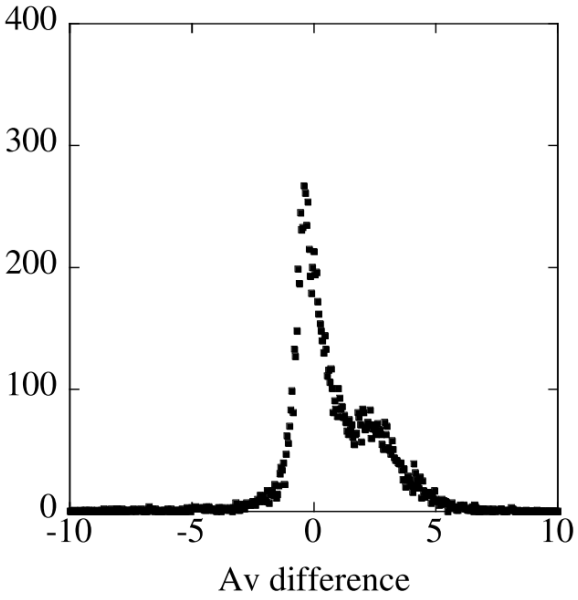

Figure 3.5: Histogram of the A_V difference of A_V (steep) – A_V (single). Bin size is 0.05 mag.

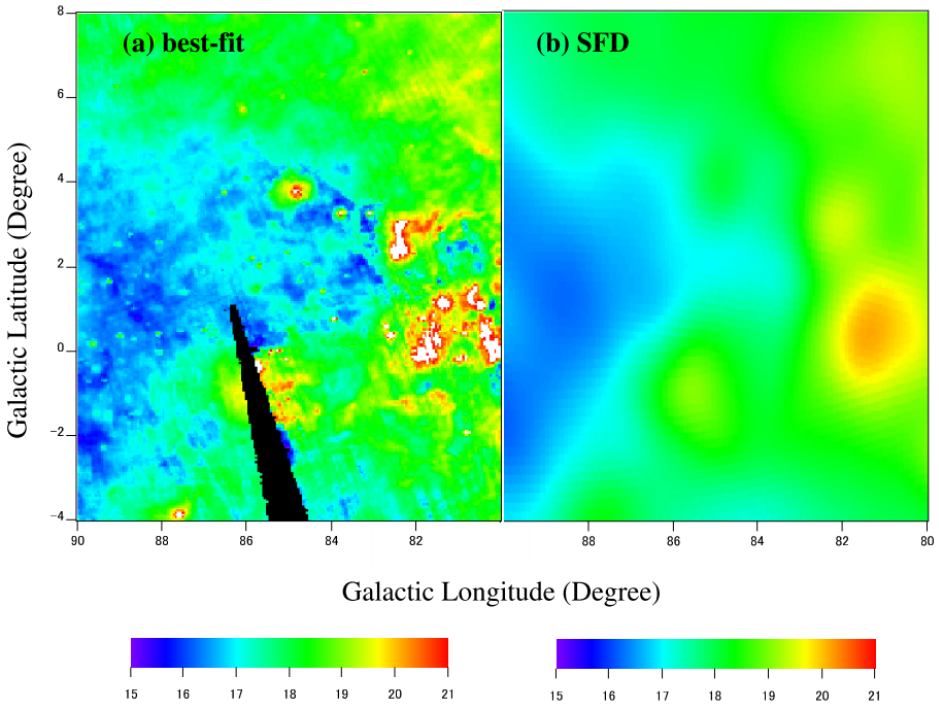

Figure 3.6: Dust temperature distribution maps in the Cygnus region [K]: (a) present study and (b) that by SFD. The black area in panel (a) indicates the area that *IRAS* did not survey.

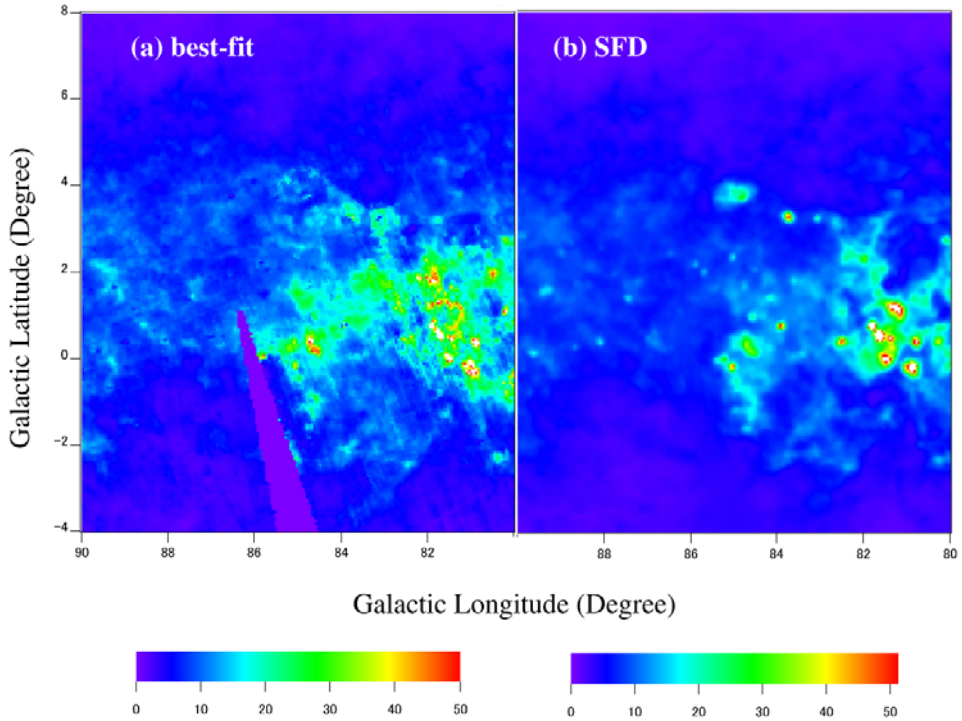

Figure 3.7: A_V distribution maps [mag]: (a) present study and (b) that by SFD.

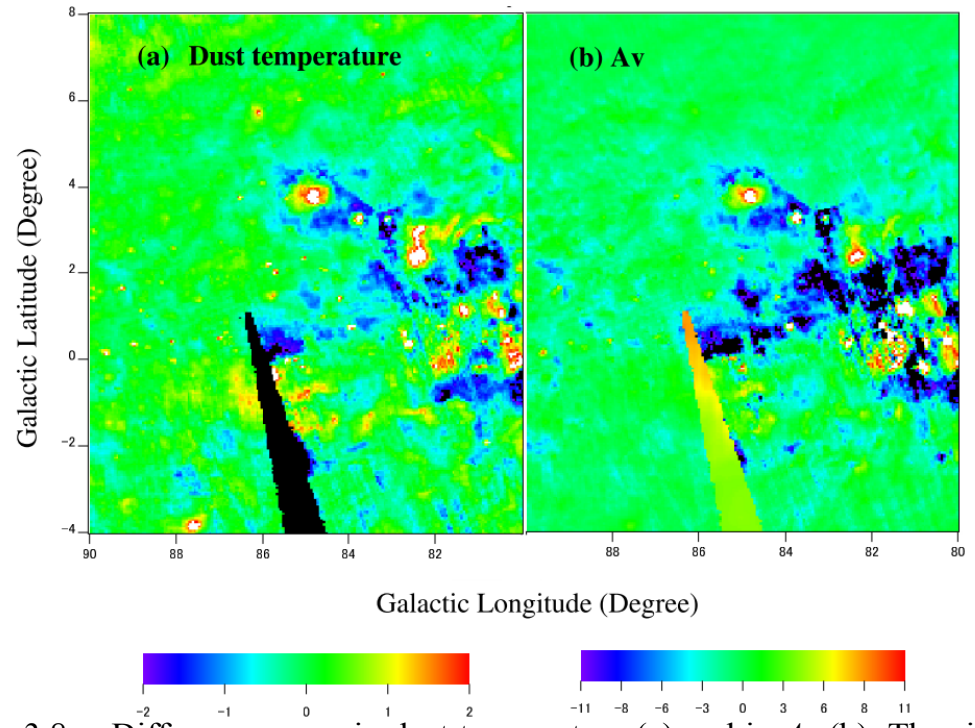

Figure 3.8: Difference maps in dust temperature (a) and in A_V (b). The sign is reversed for the left panel.

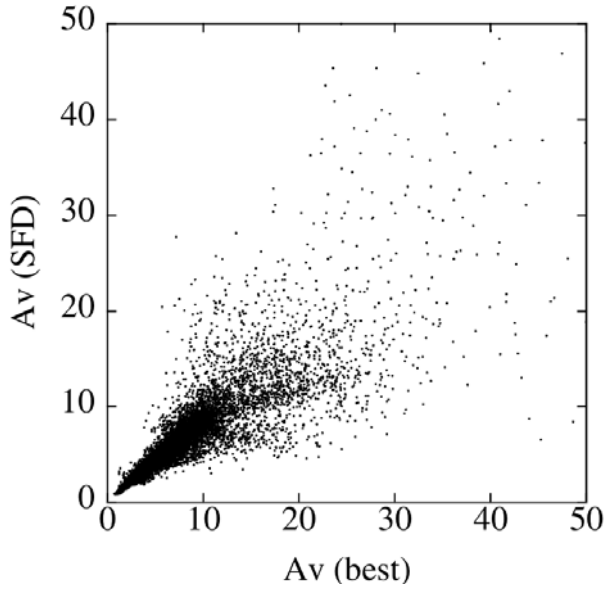

Figure 3.9: Comparison between the A_V values of the best-fit case and SFD.

3.4 Discussion

3.4.1 Comparison with SFD

The methods using the best-fit and steep cases are considered to be more precise than the SFD method because of the following reason. As described in Chapter 3.2, the A_V map derived by the best-fit differs from that by SFD, and the difference can be ascribed to the fact that the present temperature map has higher spatial resolution compared with that of SFD. Figure 3.9 shows the result of comparison between the A_V values of the best-fit case and SFD. The difference, (A_V (best) − A_V (SFD))/A_V (best), scatters by 21% in 1σ. On the other hand, the noise of the IRIS data is 0.03 and 0.06 MJysr^{-1} at 60 and 100 μm (Miville-Deschênes & Lagache 2005). These values correspond to less than 1% for A_V and are negligibly small compared to the difference between A_V (best) and A_V (SFD).

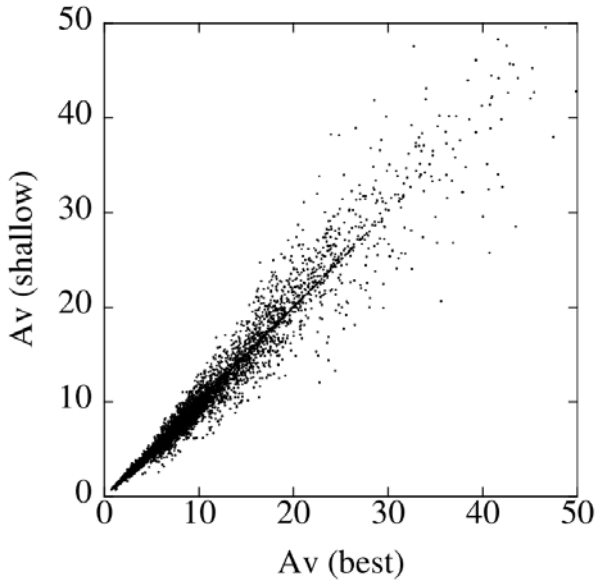

Figure 3.10: Comparison between the A_V values of the best-fit case and the shallow case.

Figure 3.10 shows the comparison between A_V (best) and A_V (shallow). It can be seen that the difference is large compared to the noise of the DIRBE data points, reflecting the fact that the power of the shallow case does not represent the entire correlation in the Cygnus region. Figure 3.11 shows the comparison between A_V (best) and A_V (steep). The difference is 5% (1 sigma of (A_V (best) □ A_V (steep))/ A_V (best)). The difference between A_V (steep) and A_V (SFD) is 20% (1 sigma of (A_V (steep) □ A_V (SFD))/ A_V (steep)). Figure 3.12 shows the comparison of A_V (steep) and A_V (single). The difference, (A_V (steep) □ A_V (single))/A_V (steep)), scatters by 21% in 1σ. It is consistent with the hypothesis described in Chapter 3.2 that the steep, shallow, and best-fit cases are more accurate compared with the single case.

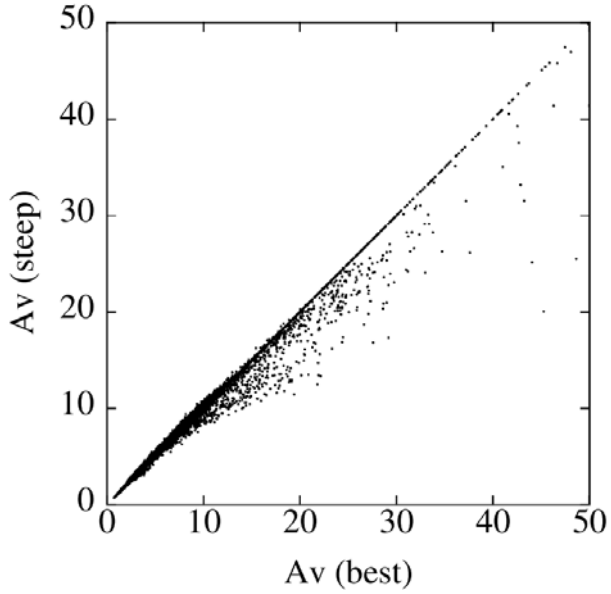

Figure 3.11: Comparison between the A_V values of the best-fit case and the steep case.

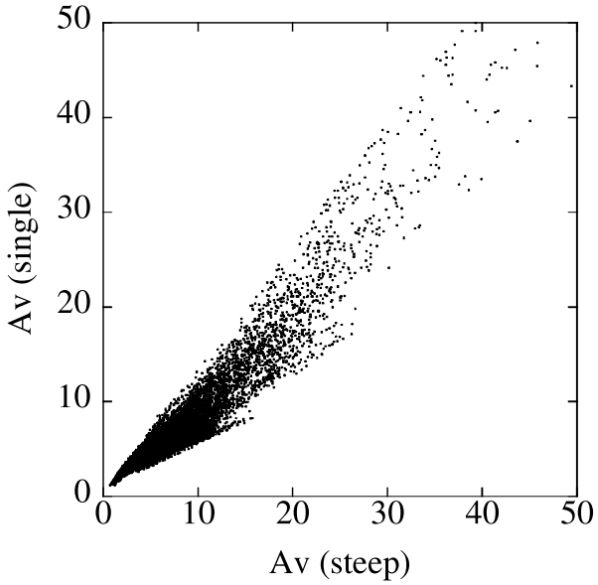

Figure 3.12: Comparison between the A_V values of the best-fit case and the single case.

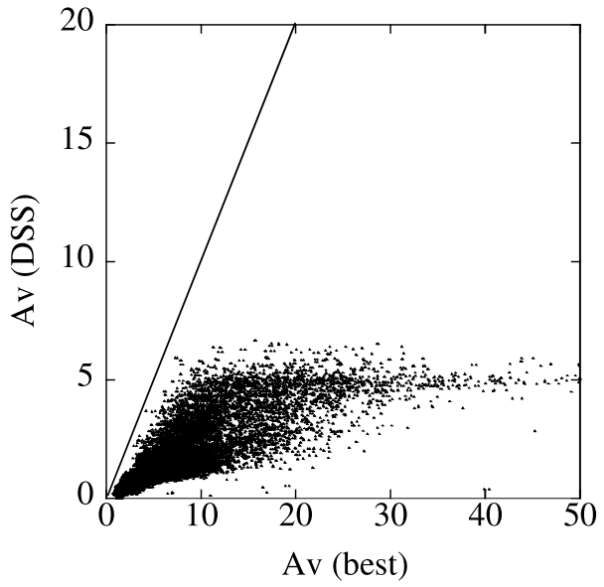

Figure 3.13: Comparison between the A_V values of the best-fit case and Dobashi et al. (2005). The solid line indicates a slope of unity.

3.4.2 Comparison with the Star Counting Method

Dobashi et al. (2005) published an A_V map within $|b| < 40^\circ$ by the star counting method using the DSS images. The spatial resolution is 6′, similar to the present study. Figure 3.13 shows the result of the comparison of both A_V data in the Cygnus region. The A_V (DSS) data is distributed lower than A_V (best) and saturated at A_V (DSS) > 5 mag. This indicates that the star counting method with DSS has a limit of around A_V (DSS) > 5 mag. It is apparent that their method is not useful for A_V > 5 mag because the optical radiation does not reach us because of heavy extinction by the dust. Dobashi (2011)'s map derived by 2MASS PSC will be compared in the later chapter 4.4.2.

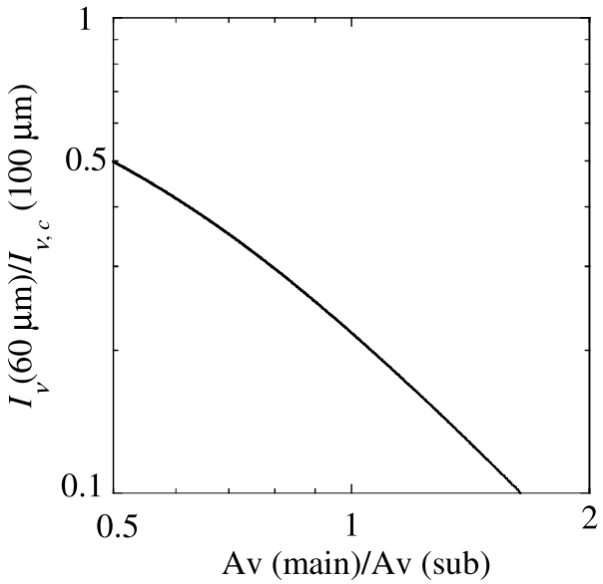

Figure 3.14: Uncertainty of A_V when the sub-correlation is adopted. The solid curve shows the ratio of A_V by the main-correlation over the sub-correlation.

3.4.3 Selecting Valid Correlation

As shown in chapter 3.3.1, A_V by the best-fit and steep cases are more precise than that by SFD in the Cygnus region. But these methods would not be effective in high Galactic latitudes because intensity at DIRBE has a lower S/N ratio in those latitudes. Therefore, if the author chooses one case only out of the best-fit, shallow, steep, the main-correlation, and the sub-correlation for the entire sky, the sub-correlation is best suited because of its similarity to the steep case. The color-color correlations in high Galactic latitudes will be shown in the latter chapter 4.2.

In the entire sky, there are regions where both the main-correlation and the sub-correlation can be seen (e.g., the Galactic plane). There are two methods for determining whether the main- or sub-correlation is applicable if the best-fit is not used. The first method is the same as that for the Cygnus region. A color-color diagram can be derived in any area of the sky and choose the better one. The second method involves referring to the radio thermal continuum map that represents the bulk of the ionized gas excited by the OB stars. The direction with strong radio continuum should be associated with the region where the ISRF varies on a small scale because of the strong local heating sources.

Therefore, the far-infrared colors in the direction with strong radio continuum can be thought to follow the sub-correlation as demonstrated by Hibi et al. (2006). Figure 3.1 shows that the sub-correlation is more major than the main-correlation in the Cygnus region. In a latter chapter (4.2.2), the two correlations are divided by all-sky radio continuum emission map at 41 GHz.

The systematic difference arising from the selection of either the main-correlation or the sub-correlation is estimated, since in general the author is unaware a priori which of the two correlations is applicable to a certain region. A_V calculated by the main-correlation and the sub-correlation are compared in Figure 3.14. The range of the A_V ratio is between 1 and 2.5 where the range of $I_{\nu,c}$ (60 μm)/$I_{\nu,c}$ (100 μm) is between 0.2 and 0.6.

3.4.4 Validity of Applying Correlations to IRAS Map

Hibi et al. (2006) identified the two groups in the color-color plot of the DIRBE data with 0˚.7 resolution. Each group has good correlation expressed by Equations (3.1) and (3.2). These two expressions can be applied to the intensity distribution with a higher spatial resolution such as that of the *IRAS* map. As indicated by Hibi et al. (2006) and Hirashita et al. (2007), the main-correlation represents the lines of sight along which the ISRF is constant, and the sub-correlation represents the lines of sight along which the ISRF varies greatly. Obviously, the lines of sight showing the sub-correlation may also represent the direction along which the ISRF varies within the beam.

The direction following the main-correlation with the DIRBE beam does not include regions having strong radiation (Case 1). Otherwise, it must follow the sub-correlation. The ISRF does not vary extensively along the line of sight and over the spatial extent of the DIRBE beam. Therefore, all lines of sight of the *IRAS* beam in a DIRBE beam should follow the main-correlation.

On the other hand, there should be strong ISRF regions in the line of sight indicating the sub-correlation with the DIRBE beam (Case 2). The strong ISRF region is usually compact, so the spatial extent could be smaller than the DIRBE beam. A DIRBE beam can be divided into many *IRAS* beams, some indicating the main-correlation (Case 2-1) and the others the sub-correlation (Case 2-2). The former does not include the strong ISRF regions, and the latter includes the strong radiation field region in the line of sight.

In Case 2-1, the difference in the derived A_V between the main-correlation and the sub-correlation must be small because there is only a small difference between the main-correlation and the sub-correlation under weak ISRF. If the sub-correlation is applied, the maximum error of A_V is 30%, where IRAS60/IRAS100 is lower than 0.3 (Fig. 3.14).

Finally, Case 2-2 is considered. The *IRAS* data points that include a strong radiation field in the DIRBE beam also follow the sub-correlation, because such a strong radiation field does not entirely occupy the line of sight. Therefore, there is no error in using the sub-correlation in Case 2-2.

Consequently, even if a higher spatial resolution map (e.g., *IRAS*) is employed, the A_V error does not increase to a large extent.

3.5 Summary

A_V map with 5′ resolution in the Cygnus region has been derived assuming the color–color correlation between 60, 100, and 140 μm discovered by Hibi et al. (2006). The difference may occur because the spatial resolution of the present temperature map is 10 times higher than that of SFD. Therefore, the present method is more accurate than that of SFD. The A_V difference between the present study and SFD is significantly larger than the uncertainty associated with the derivation of the intensity at 140 μm with 5′ resolution in the present study.

Chapter 4

A Galactic Extinction Map in High Galactic Latitudes

In this chapter, the method of the present study is applied to a region of high ecliptic latitudes with $|\beta| > 30^{\circ}$. The extinction map derived in this chapter is compared with those of SFD and Dobashi (2011). The difference between this work and SFD in high galactic region is expected to be smaller than the difference between the extinction map of the Cygnus region and SFD. It is because that the fact that the dust distribution in high galactic latitudes is more uniform than that in the galactic plane. The difference between this work and Dobashi (2011) is also expected to be smaller than the difference between the extinction map of the Cygnus and Dobashi (2005). It is because that the near-infrared study in Dobashi (2011) allows to detect a larger extinction using the color excess of more distant stars than the optical work by Dobashi et al. (2005).

Content of this Chapter is summarized as a paper and submitted to Publication of the Astronomical Society of Japan (PASJ).

4.1 Far-Infrared Data Process

In order to avoid pixel distortion, the far-infrared data of *IRAS* and DIRBE are reprojected to the HEALPix projection, which is a suitable projection method to represent the all-sky data. In addition, the CIB radiation contribution is removed on the basis of the results of previous studies. It is because that CIB's contribution is significant to the far-infrared intensity in high galactic latitudes.

4.1.1 Projection Method

All data are presented in the Hierarchical Equal Area isoLatitude Pixelization (HEALPix) projection (Górski et al. 2005). The pixel scale in this work is set as large as 1′.7 that is corresponds to Nside = 2048; Nside is the pixel scale parameter of the HEALPix projection. The HEALPix pixel scale has previously een defined discretely (Górski et al. et al. 2005, Table 1). The images of IRIS, which is used as the *IRAS* image in this study, available in the HEALPix projection with a 1′.7 pixel scale. As described in Chapter 2, the images of ZSMA, which is used as the DIRBE image in this study, are available in the Quadrilateralized Spherical Cube (QSC) projection and the data are binned to 393,216 pixels with a 19′.5 pixel scale. The direct transformation from the QSC to HEALPix 1′.7 pixel size was found to be inappropriate because it produced blank pixels and forced interpolations during the reprojection process. Therefore, the QSC data were first reprojected to the HEALPix projection with a 27′.5 pixel scale (Nside = 128).

Because the ZSMA images need to be spatially smooth to achieve sufficient S/N, conversion to the larger pixel size was not a disadvantage for this work as (described in Chapter 4.2.1 for detail). The images with the pixel size of 27′.5 were regridded to a 1′.7 pixel scale as those of *IRAS*. The images were smoothed with a Gaussian of 30′ FWHM to reduce the jagged pattern caused by reprojection.

Table 4.1: CIB intensities at 60, 100, 140 μm

Wavelength [μm]	Intensity [MJrsr^{-1}]	Reference
60	0.27 ± 0.05	Miville-Deschênes, Lagache, & Puget (2002)
100	0.73 ± 0.03	Planck collaboration (2011)
140	0.94 ± 0.16	Matsuura et al. (2011)

4.1.2 CIB contribution Subtraction

The offsets of the Cosmic Infrared Background (CIB) radiation at the three wavelengths were subtracted. The CIB intensities employed in this work, shown in Table 4.1, are lower than the upper limit indicated by Hauser et al. (1998).

4.2 Color-Color Correlations in high galactic latitudes

Hibi et al. (2006) analyzed the ZSMA data in the galactic plane ($|b| < 5^\circ$) and identified two color-color correlations at 60, 100, and 140 μm. As described in Chapter 3, the author analyzed the ZSMA data in the Cygnus region and identified two correlations that differed slightly from those identified by Hibi et al. (2006) (Chapter 3). In this work the ZSMA were also analyzed. Then two correlations were identified in the region with $|\beta| > 30^\circ$. The high galactic latitude region was included in this analysis. The S/N of DIRBE140 is lower than that of DIRBE60 and DIRBE100. In addition, the S/N of DIRBE140 in high galactic latitudes is lower than that in the galactic plane. Therefore, the DIRBE maps were smoothed spatially with a Gaussian filter to improve the S/N of DIRBE140.

Table 4.2: Summary of the spatial smoothing process to achieve the S/N of DIRBE 140 over 10

S/N ratio before the smoothing	FWHM of a Gaussian [deg]	Spatial resolution after the smoothing [deg]	Expected S/N ratio improvement
> 10	□	0.9	×1
5□10	1.5	1.8	×2
2.5 □ 5	3.4	3.6	×4
1.3 □ 2.5	7	7.2	×8
< 1.3	13.8	14.4	×16

4.2.1 Smoothing of DIRBE maps and Identification of Color-Color Correlations

As shown in Table 4.2, the FWHM of the Gaussian was changed depending on the S/N of DIRBE140 because of the fact that the maps smoothed with a large beam have the disadvantage of throwing away small-scale information in the regions in the high-S/N regions.

Figure 4.1 shows S/N distribution of DIRBE140 after the processes described in Chapter 4.1.1. The FWHM of the Gaussian is defined to achieve an S/N of DIREB140 over 10. Tight relations such as the main-correlation and sub-correlation are expected in this case because the S/N of DIREB140 in the region analyzed by Hibi et al. (2006) is over 10. The 1σ noise levels of DIRBE140 are 1.4 MJysr$^{\square 1}$ after the processes described in Chapter 4.1.1 and 2.4 MJysr$^{\square 1}$ in the QSC projection (DIRBE explanatory supplement 1998).

Figure 4.2 shows the color-color diagram in the region with $|\beta| > 30^{\circ}$. The Galactic and the Magellanic cloud data points are shown and color-corrected. The regions of the LMC and SMC were defined as those IRAS100 is over 10 MJysr$^{\square 1}$ and 3 MJysr$^{\square 1}$ in the directions of LMC and SMC, respectively.

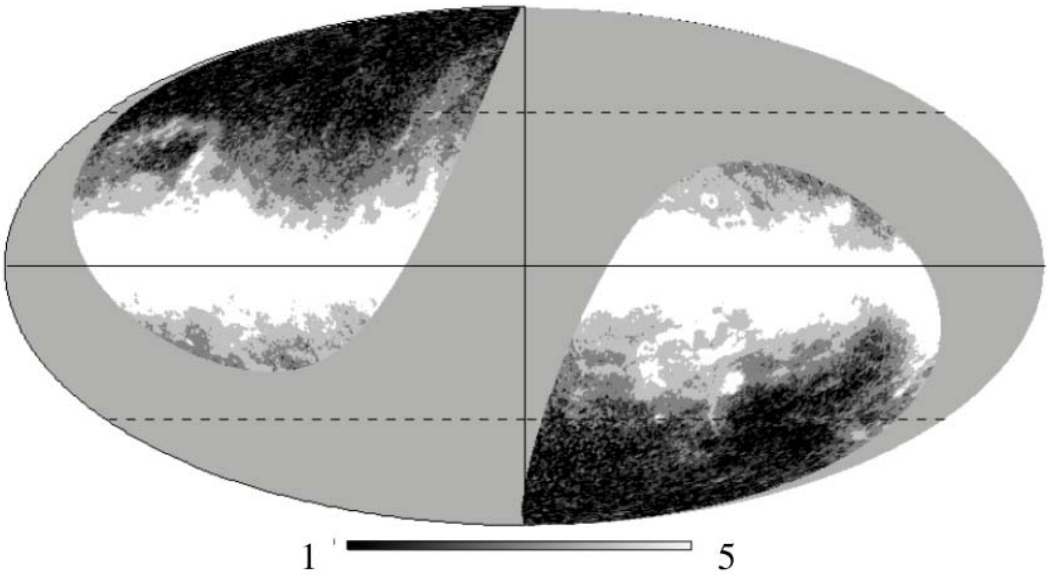

Figure 4.1: Map of the S/N of DIRBE140, which was divided into five classes. The white region represents classes with S/N ratios higher than those of the black region; the gray zone represents the region that within | β | < 30˚. The distribution is shown in the Mollweide projection with the galactic coordinate. The dotted lines indicate the galactic latitudes of | *b* | = 45˚.

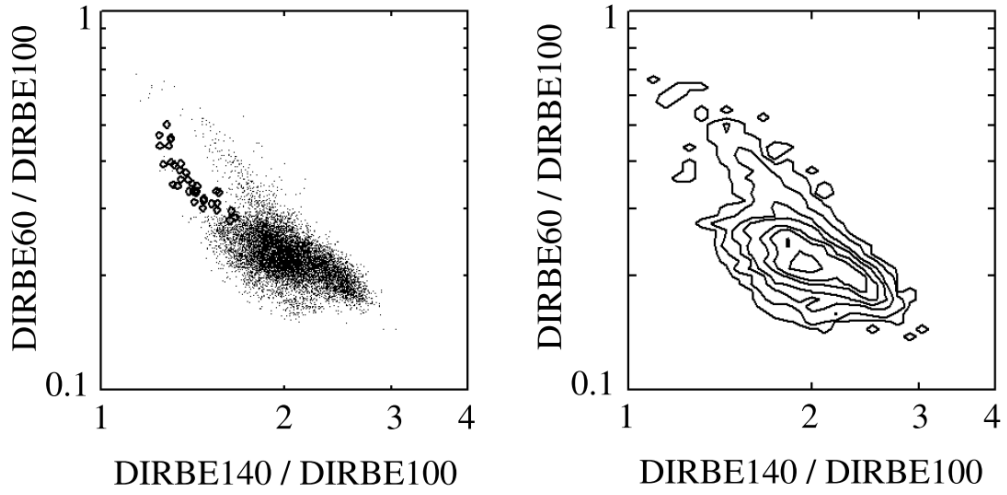

Figure 4.2: (left) Color-color diagram of the region with | β | > 30˚. The DIRBE maps were smoothed to achieve an S/N of DIRBE140 over 10. The dots and squares represent Galactic and Magellanic data points, respectively. (right) The contour map demonstrating the density of the data points on the diagrams. The bin sizes is set to be 0.02 in logarithmic units. Contour lines are drawn according to the number of data points, including 0.5 (to express the boxes which have only one data point), 0.1N, 0.5N, N, 2N, 3N, and 5N on the diagram, where N = 40, indicates the average number of data points contained in each bin on this contour map.

4.2.2 Division of Color-Color Correlation

Hibi et al. (2006) separated the two correlations by using the 10 GHz radio continuum emission map (□4° < l < 56°, |b| < 1°.5) produced by Handa et al. (1987). Hibi et al. (2006) and Hirashita et al. (2007) indicated that the inclination of the correlation in the color-color diagram changes depending on the free-free emission intensity in a line of sight. The two correlations were separated by using *the Wilkinson Microwave Anisotropy Probe* (*WMAP*; *WMAP* Seven-Year Explanatory Supplement) all-sky map at 41 GHz produced by Jarosik et al. (2011).

Two color-color diagrams are presented in Figure 4.3 with antenna temperatures lower and higher than 0.7 mK at 41 GHz. The former exhibited shallower inclination than the latter. Similar to the color-color correlation in the Cygnus region (Chapter 3), the former and latter are described as shallow and steep cases, respectively. The correlation coefficient of the shallow and the steep cases are □0.6 and □0.8, respectively. The two color-color diagrams appeared to show tight relations. In addition, the results of Hibi et al. (2006) and the Cygnus region are shown. Hibi et al. (2006) separated the two correlations at an antenna temperature of 0.5 K at 10 GHz. The 10 GHz radio continuum emission map is available only within a limited region; therefore, the 41 GHz radio continuum emission map is more useful for separating the correlations because it is available for all-sky. As the 10 GHz radio continuum emission, the 41 GHz radio continuum emission mainly dominated by free-free emission from an ionized hydrogen cloud (HII region).

In the Cygnus region, the two correlations were separated at the DIRBE60/DIRBE100 ratio is 0.28. In contrast to the value of the antenna temperature at 41 GHz, a certain value of the DIRBE60/DIRBE100 ratio cannot separate the two correlations shown in Figure 4.2.

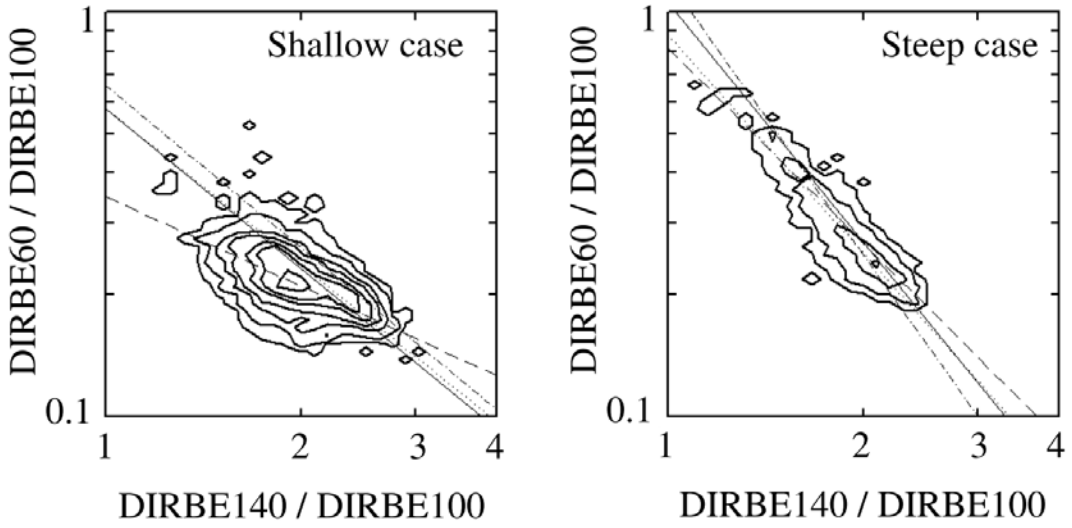

Figure 4.3: Two color-color diagrams of the region with | β | > 30˚. (left) 41 GHz antenna temperature below 0.7 mK; (right) 41 GHz antenna temperature over 0.7 mK. Solid and dashed lines show the color-color correlations for cases I and II, respectively; dotted lines show the result in the Galactic plane (Hibi et al. 2006) with the main-correlation in the left and the sub-correlation in the right; and dotted-dashed lines show the result in the Cygnus region (Chapter 3). The 41 GHz radio continuum emission map was not used by Hibi et al. (2006) or in the Cygnus region to separate the two correlations they identified. The contour map includes the same parameters as those described in Figure 4.2.

4.2.3 Fitting

The color-color correlations are fitted by a power-law function using the least squares method with parameters of coefficient and power in the two color-color diagrams (Figure 4.3), and provide the results summarized in Table 4.3. In the fitting process, we try two cases for the fitting: for case I, each data is given a weight according to its 1σ photometric error and for case II no weights is applied. As described in Chapter 3.2, only the power-law index *b* will be used but the coefficient *a* will not in the following discussion (see Eq.(3.5)).

The fitting results are shown in the color-color diagrams in Figure 4.3. As seen in the right panel of Figure 4.3, the slopes of the power-law function are similar among cases I and II and previous studies. However, the difference between cases I and II is significant for the shallow cases as shown in the left panel. Case I represents the correlation of the DIRBE data with a relatively high S/N (over 10 for DIRBE140) that concentrates to the galactic plane. Therefore

case I is considered to represent the correlation of the galactic plane. This is reasonable since the slope of case I is consistent with that of Hibi et al. (2006) and the Cygnus region, which were derived for the galactic plane. On the other hand, data with relatively high and low S/N were mixed in case II. Data with lower S/N were observed in high galactic latitudes. The lower S/N does not indicate that the values should be neglected since the S/N ratio itself is sufficient for discussion (S/N over 10 for DIRBE140).

Figure 4.4 shows color-color diagrams for the shallow case at different galactic latitudes. In the galactic plane ($|b| < 5^\circ$), the inclination of the color-color correlation is similar with that of case I rather than case II. In contrast to the galactic plane, the inclination of the color-color correlation in high galactic latitudes is similar with that of case II rather than case I. Even though the inclination actually depends on the galactic latitudes, its dependency is not clear. For example, the DIRBE data points in the middle galactic plane ($5^\circ < |b| < 20^\circ$) seem to follow both case I and case II.

Table 4.3: Fitting results of the color-color correlation by a power-law function

Case	Shallow case	Steep case
Case I weighted least squares fitting ($\|\beta\| > 30^\circ$)	$a = 0.659 \pm 0.003$ $b = -0.767 \pm 0.003$	$a = 1.03 \pm 0.02$ $b = -0.508 \pm 0.004$
Case II un-weighted least squares fitting ($\|\beta\| > 30^\circ$)	$a = 0.24 \pm 0.02$ $b = -1.36 \pm 0.02$	$a = 0.88 \pm 0.07$ $b = -0.627 \pm 0.001$
Cygnus region derived in Chapter 3 ($80^\circ < l < 90^\circ$, $-4^\circ < b < 8^\circ$)	$a = 0.73$ $b = -0.78$ (Eq. 3.3)	$a = 1.09$ $b = 0.56$ (Eq. 3.4)
Hibi et al. (2006) Galactic plane ($\|b\| < 5^\circ$)	$a = 0.65$ $b = -0.78$ (main-correlation; Eq. 3.1)	$a = 0.93$ $b = -0.56$ (sub-correlation; Eq. 3.2)

Parameters a and b are the coefficient the power of power-law function, respectively. Errors of Case I & II are shown in 1σ.

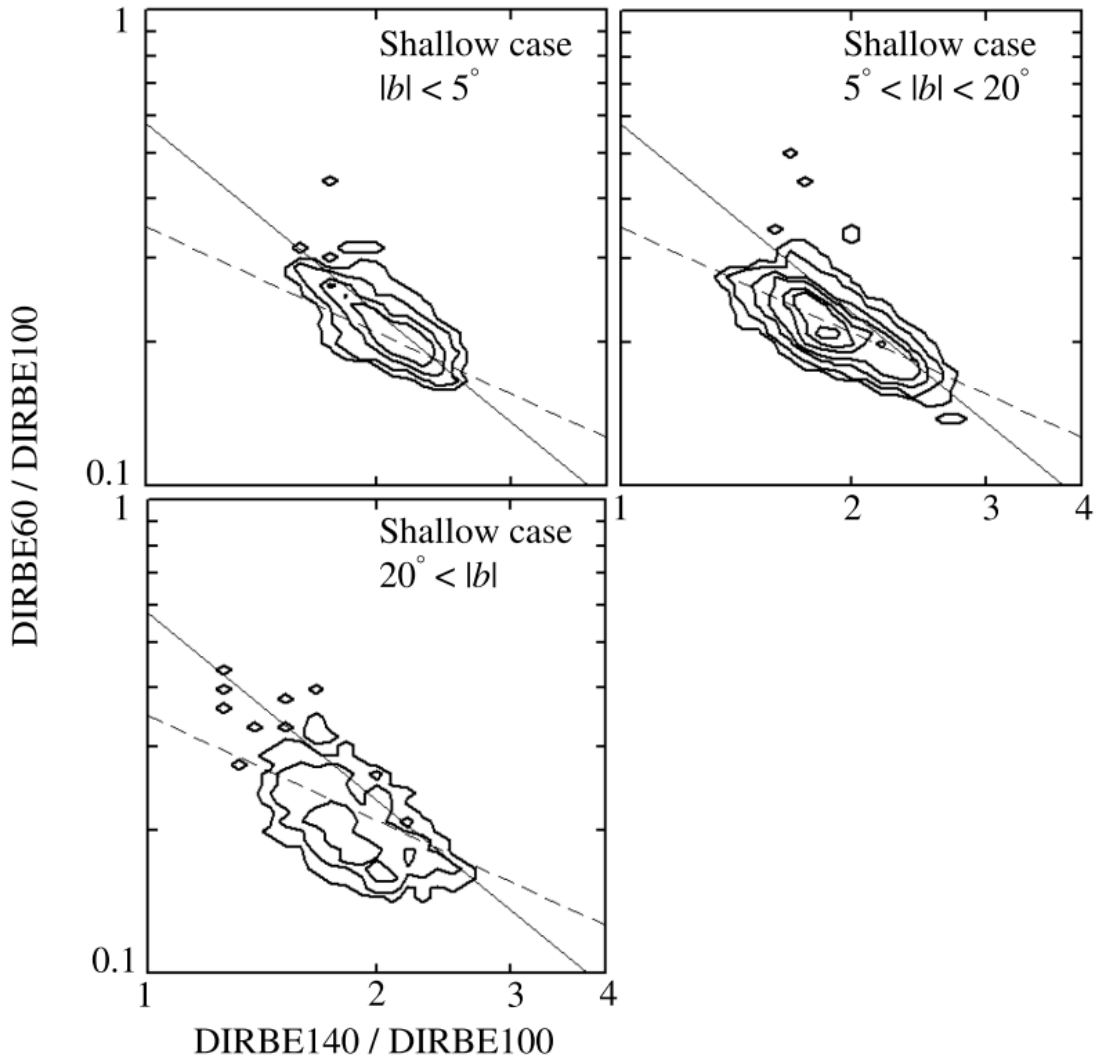

Figure 4.4 : Color-color diagrams for the shallow case. Each panel shows a diagram at different galactic latitudes. The contour map includes the same parameters as those described in Figure 4.2. Solid and dashed lines are the same as shown in Figure 4.3.

4.2.4 Uncertainty of the Interplanetary Dust Emission Subtraction

Appropriate subtraction of IPD emission is difficult to achieve because the IPD emission alone has not been observed. The region with $|\beta| < 30^\circ$ were not analyzed in order to avoid an uncertainty of the IPD emission subtraction, which originates from the systematic stripe features appeared in DIRBE60 (and IRAS60) in the ecliptic plane (DIRBE60; Hauser et al. 1998; IRAS60; Miville-Deschênes & Lagache 2005). Kelsall et al. (1998) predicted the IPD emission with 1% precision; however, uncertainty of the stripe feature is considerably significant. For example, such uncertainty is about 50% at the ecliptic latitudes of 180°. The average of DIRBE60 adjacent the stripe is 0.6 $MJysr^{-1}$ and inside the stripe is 0.3 $MJysr^{-1}$.

4.3 Galactic Extinction Map

IRAS140, dust temperature, and extinction were derived for cases I and II. IRAS140 was derived by Equation (3.5). The calculation method was the same as described in Chapter 3.2 except for the power-law values of the color-color correlations. The power-law values were determined on the basis of the antenna temperature at 41 GHz in a line of sight. The dust temperature was derived from intensities at 100 and 140 μm, and the optical depth at 100 μm was derived from the dust temperature and the intensity at 100 μm. The optical depth was converted to the extinction at V band (i.e., A_V) assuming the extinction law of Mathis (1990).

Figure 4.5 and Figure 4.6 illustrate maps of dust temperature and extinction, respectively. The notations for A_V shown in this work are summarized in Table 4.4.

The results based on the case I is employed, and the difference between the case I and the case II is added in the A_V uncertainty of this work based on the following reasons. The correlations in case I are considered to represent a common dust property as described below. The color-color correlations of case I

Table 4.4: Calculation methods for A_V

Notation	Method
A_V(case I)	present study method, assuming case I (see Table 4.3)
A_V(case II)	present study method, assuming case II (see Table 4.3)
A_V(SFD)	same as Table 3.1 i.e., Schlegel, Finkbeiner, & Davis (1998; SFD)
A_V(2MASS)	Dobashi (2011)

are similar to the correlations identified by Hibi et al. (2006) and those of extragalaxies. Hibi et al. (2006) found that the color-color correlation of the Magellanic clouds were similar to the main correlation, which is the shallow case of Hibi et al. (2006). The shallow case I correlation is found to be similar to the main-correlation. Moreover, Hirashita and Ichikawa (2009) found that the color-color correlations of the blue compact dwarf galaxies are similar to the correlations identified by Hibi et al. (2006).

In both shallow and steep cases, the difference between case I and case II is larger than that between case I and Hibi et al. (2006) and that between case I and the correlations of the Cygnus region. As demonstrated in Chapter 4.4, the A_V differences between SFD and the result for case I and that between Dobashi (2011) and the result for case I are significant even if the difference between the results for cases I and II is added in the A_V uncertainty of this work. A significant difference is also expected even if differences between the results for case I and Hibi et al. (2006) and that between the results for case I and the correlations of the Cygnus region are added to the A_V uncertainty.

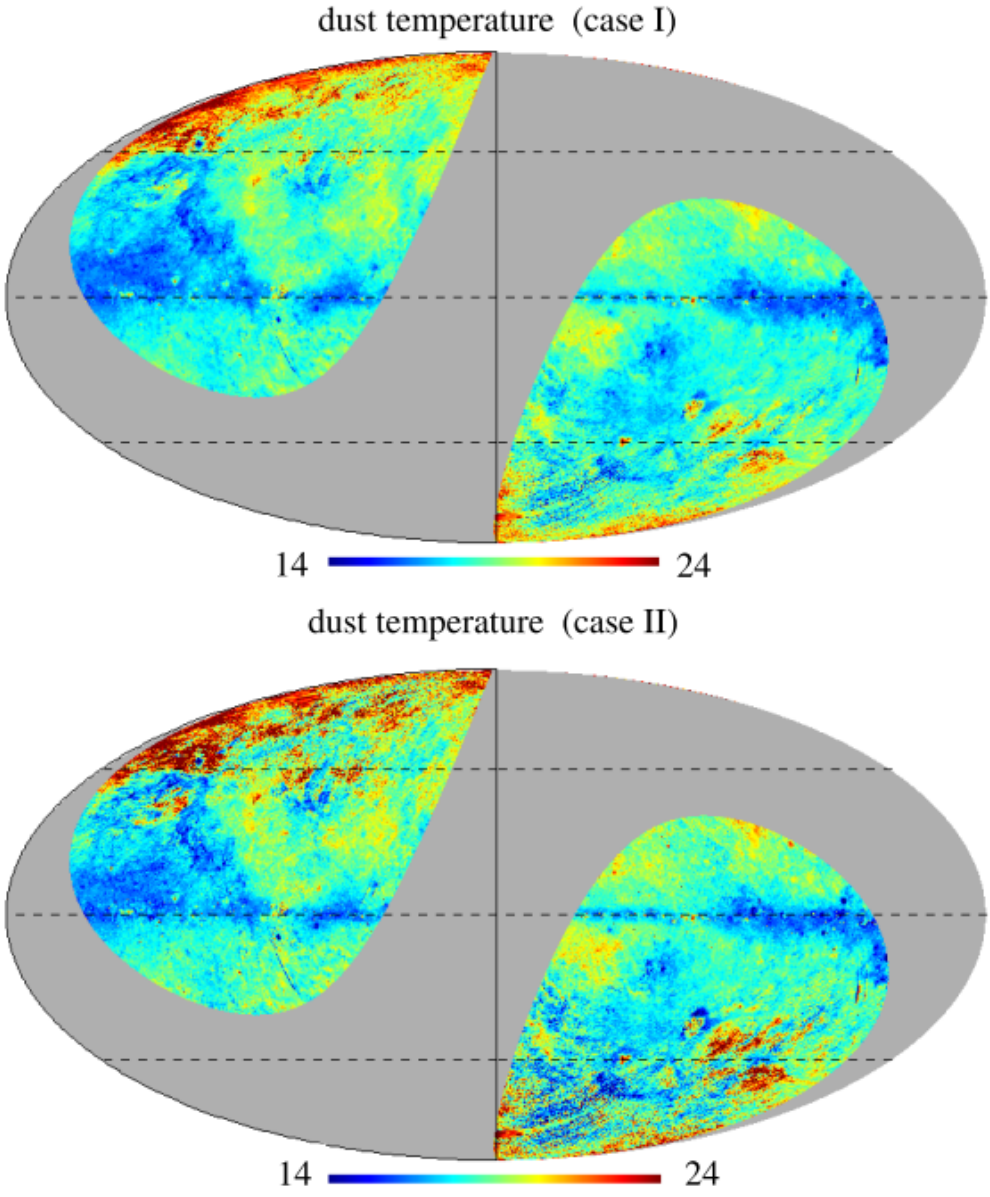

Figure 4.5: Dust temperature distribution [K]. Top and bottom columns show results for cases I and II, respectively.

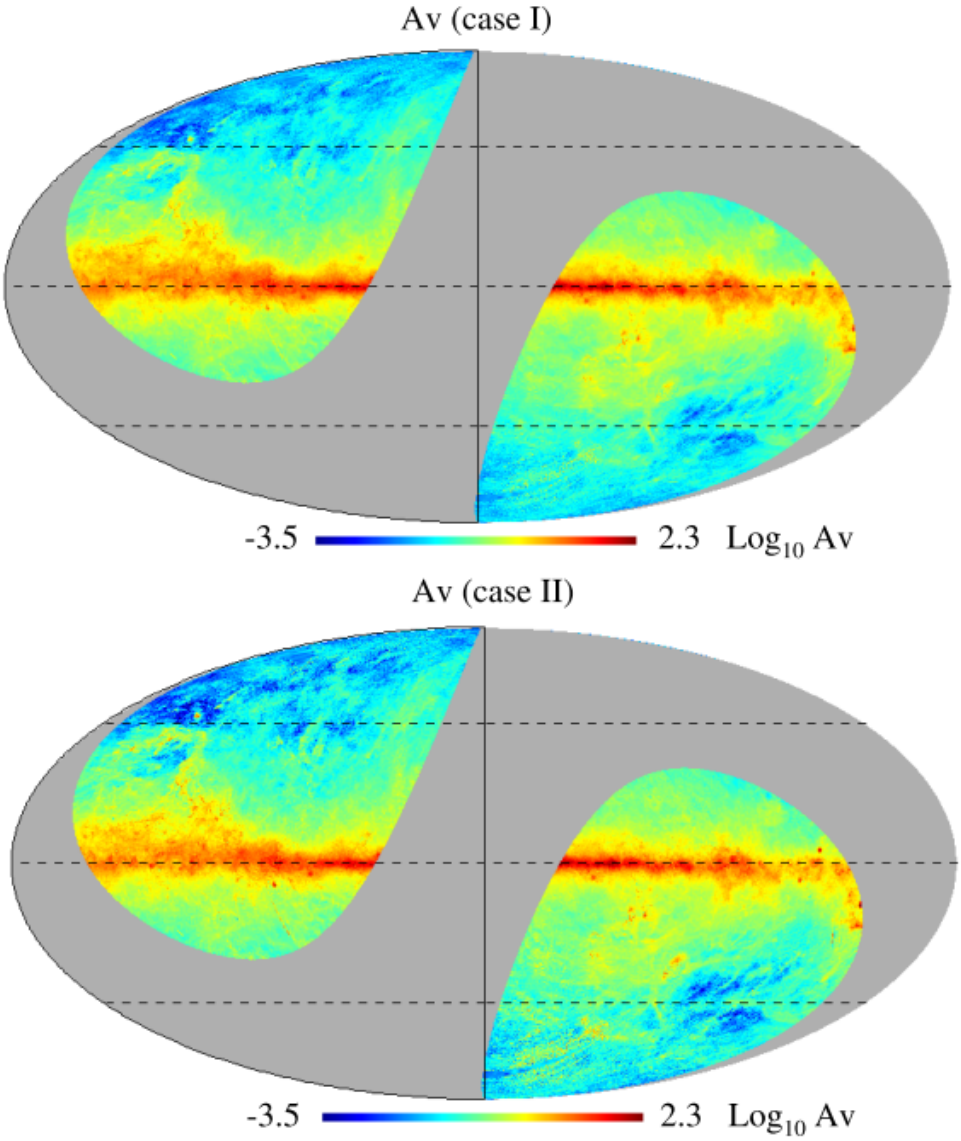

Figure 4.6: Galactic extinction distributions at V band [mag]. Extinction is shown in a common logarithm scale. Top and bottom columns show the results for cases I and II, respectively.

4.4 Results and Discussion

As described above, the maps of dust temperature and extinction were derived with the 5′ spatial resolution on the basis of far-infrared intensities. As shown below, the derived extinction map based on case I was compared with the maps of SFD and Dobashi (2011). The method of this work is as accurate as that of SFD and is more precise with respect to the higher spatial resolution of the dust temperature. In addition, the method of this work has an advantage over that of Dobashi (2011) regarding high extinctions towards extragalaxies since the extinction map derived in this work is based on the far-infrared radiation which can trace the region of large optical depth.

4.4.1 Comparison with SFD

The difference in the spatial resolution of the dust temperature is expected to create a scatter difference between this work and SFD but not cause a systematic difference. This method's accuracy is estimated assuming that SFD's map is correct in a 1° or larger spatial scale. In addition, the author assumes that the difference in spatial resolution of the dust temperature causes a scatter difference only.

Figure 4.7 shows the comparison between the A_V values of case I and SFD, in which a scatter difference is evident. A_V (SFD) is derived from the E (B□V) of SFD assuming R_V = 3.1. A systematic difference appears particularly in A_V (SFD) > 1 mag. The mean and median of the A_V (case I)/A_V (SFD) ratio in A_V (SFD) < 1 mag are 1.05 and 0.96, respectively. On the other hand, A_V (case I) is systematically larger than A_V (SFD) in A_V (SFD) > 1 mag. The mean and median of the A_V (case I)/A_V (SFD) ratio in A_V (case I) > 1 mag are 1.21 and 1.13, respectively. On the basis of the assumption described above, the accuracy of A_V (case I) is estimated to be as much as 5% and 21% where A_V (SFD) is smaller and larger than 1 mag, respectively.

The area where A_V (SFD) > 1 mag corresponds to the galactic plane ($|b| < 10°$) and the systematic difference where A_V (SFD) > 1 mag is seen there. As qualitatively-described below, this systematic difference may be caused by the

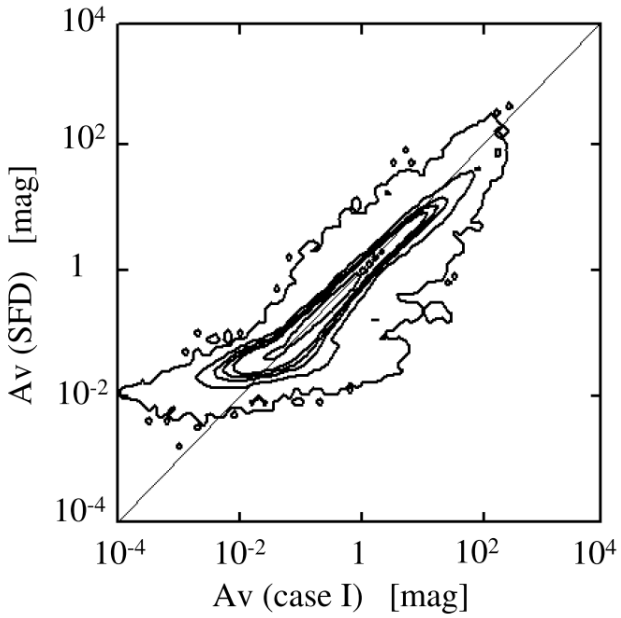

Figure 4.7: Comparison between A_V of this work and SFD. The systematic difference is 5% and 21% where A_V (SFD) is lower and higher than 1 mag, respectively. The wider scatter in A_V (SFD) < 0.1 mag may reflect an SFD assumption (see text). The contour map includes the same parameters as those described in Figure 4.2. The bin size is set to be 0.1 in logarithmic units. Contour lines are drawn according to the number of data points, including 0.5, 0.1N, 0.5N, N, 2N, and 10N on the diagram, where N = 1525 indicates the average number of data points. The solid line indicates the slope of unity.

improvement of the dust temperature resolution. Low temperature area is dominant in the galactic plane (Sodroski et al. 1997). High temperature area is not dominant. The present study derived the area with higher temperature than SFD's result. This higher temperature region is not dominant, but the area with lower temperature than SFD's result is dominant. Lower temperature area corresponds to larger extinction area. The area with larger extinction than SFD' result is considered to be dominant in the galactic plane.

It should be note that the calibration accuracy of SFD is not confirmed in A_V (SFD) > 1 mag, as described below. SFD calibrated the dust column density value into the color excess by using the reddening-MgII index relation of elliptical galaxies cataloged in Faber et al. (1989). They assured the accuracy of their method, which included uncertainties of CIB and IPD emission subtraction, absolute calibration errors, and the photometric noise of the far-infrared data (i.e., the DIRBE and *IRAS* data). In addition, SFD used the reddening-MgII index relation if the galactic extinction value was estimated by Burstein & Heiles (1978, 1982) in a line of sight. The number of the elliptical galaxies was small in high-extinction region. The sample did not appear in E (B□V) > 0.3

mag

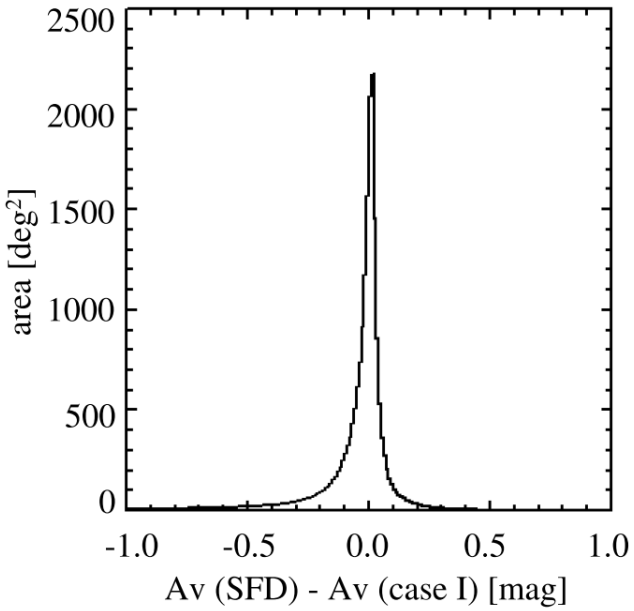

Figure 4.8: Histogram of the A_V difference between this work and SFD. Bin size is 0.01 mag. The mean, median, and standard deviation are −0.28, −0.001, and 2.29 mag, respectively.

(SFD). E (B□V) mag corresponds to A_V = 1 mag if R_V = 3.1 is assumed.

The difference in the spatial resolution of the dust temperature contributes to the horizontal scatter in Figure 4.7; this trend changes at A_V (SFD) = 0.1 mag. The horizontal scatter in A_V (SFD) < 0.1 mag becomes relatively wider than that in A_V (SFD) > 0.1 mag. The wider scatter may be caused by SFD's assumption that dust temperature is uniform in the small extinction region (i.e., in high galactic latitudes), thereby they combined the DIRBE maps with background averages obtained at high galactic latitudes with $|b| > 75^\circ$. No such assumption was applied in the method of this work.

Figure 4.8 shows a histogram of A_V (SFD) vs. A_V (case I). The mean, median, and standard deviation are □0.28, □0.001, and 2.29 mag, respectively. Figure 4.9 shows the A_V difference distribution of A_V (SFD) vs. A_V (case I). The absolute A_V difference between A_V (case I) and SFD in high galactic latitudes is smaller than that in the galactic plane because of the smaller extinction in high galactic latitudes. In addition, the dust distribution in high galactic latitudes is more uniform than that in the galactic plane, and the standard deviation in high galactic latitudes is absolutely smaller than that in the galactic plane. The standard deviation is 0.10 mag for $|b| > 45^\circ$ and 2.66 mag within $|b| < 45^\circ$.

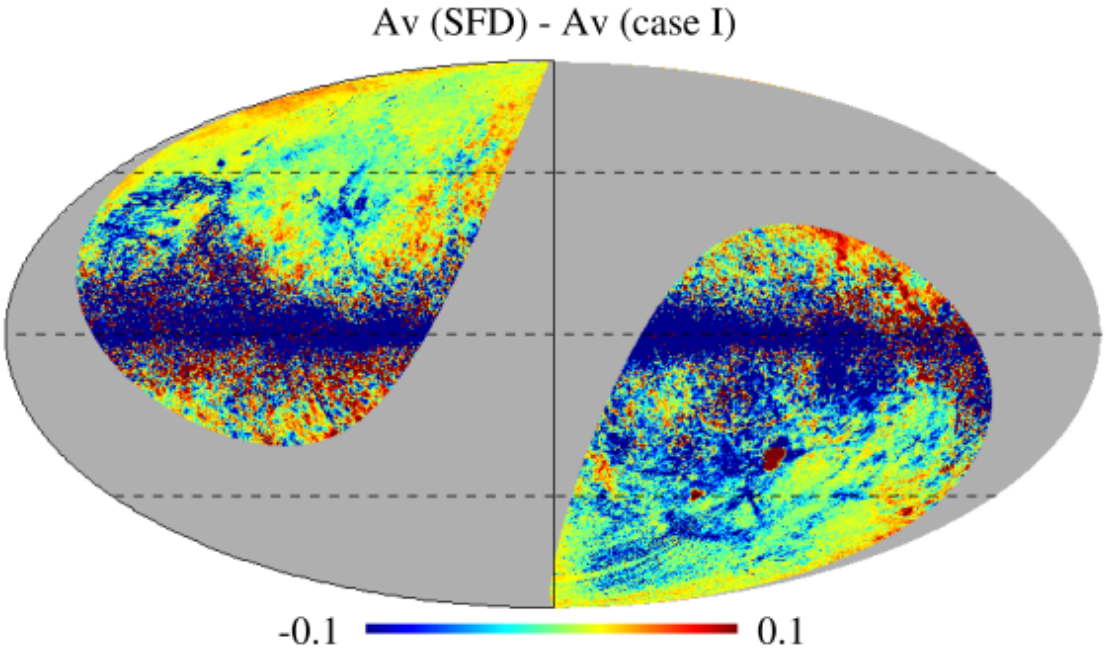

Figure 4.9: Maps of the A_V difference between this work and SFD. The range is ± 0.1 mag.

Figure 4.10 shows the A_V uncertainty of the method of this work estimated by the following equation:

$$\Delta A_V = \Delta(\text{noise}) + \Delta(\text{case I} - \text{case II}) + \Delta(\text{accuracy of this work}). \quad (4.1)$$

The first term is the A_V 1σ noise error calculated from the IRIS 1σ noise at 60 and 100 μm. Photometric noise could cause the horizontal scattering in Figure 4.7 in addition to the difference in spatial resolution of dust temperature. The second term is A_V difference between A_V (case I) and A_V (case II) calculated as $|A_V$ (case I) □ A_V (case II)|. The third term is the accuracy of the case I estimated by the systematic difference between this work and SFD. The third term is given by $0.05A_V$ (SFD) and $0.21A_V$ (SFD) for A_V (SFD) < 1 and A_V (SFD) > 1 mag, respectively. The extinction value should be estimated by the method of this work rather than by SFD's method if the scatter difference is larger than this work's A_V uncertainty in a line of sight. Figure 4.11 shows the area in which the A_V difference between this work and SFD is larger than A_V uncertainty of this work, as shown in the following equation:

$$\left|A_V(\text{SFD}) - A_V(\text{case I})\right| > \Delta A_V. \quad (4.2)$$

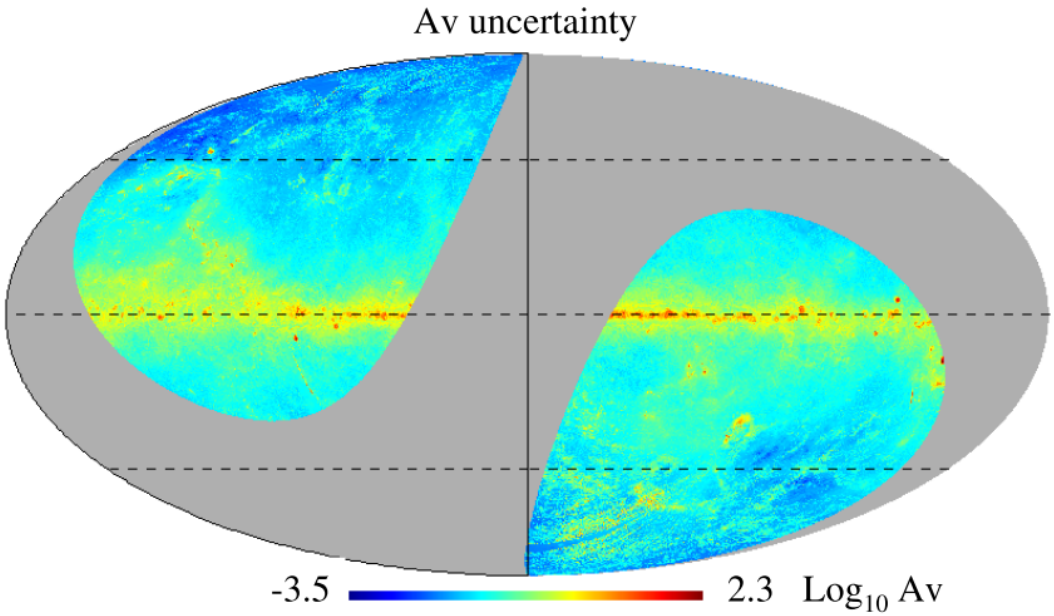

Figure 4.10: Map of the A_V uncertainty of this work estimated by Equation (4.1) [mag]. The value is shown in a common logarithm scale.

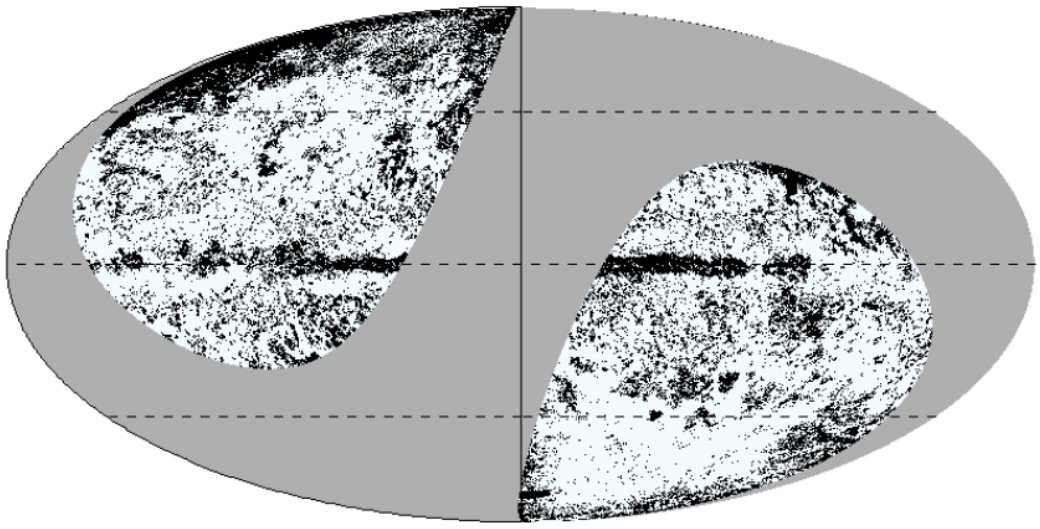

Figure 4.11: Area in which the significant difference between this work and SFD is confirmed. Black shading represents areas in which the difference is larger than the A_V uncertainty of this work. The area occupies 28% of the region with $|\beta| > 30^\circ$.

The area represented in Figure 4.11 occupies 28% of the region with $|\beta| > 30^\circ$ and exists not only in the galactic plane but also in high galactic latitudes. The area in which the significant difference is confirmed becomes larger if the author take case I or case II because the second term in Equation (4.1) is not considered. If case I only is taken, the area occupies 49% of the region with $|\beta| > 30^\circ$.

4.4.2 Comparison with Dobashi (2011)

A_V (2MASS) is converted from E ($J-H$) derived by Dobashi (2011) assuming the extinction law of Cardelli, Clayton, and Mathis (1989). E ($J-H$) is the most sensitive quantity in the color-excesses derived by Dobashi (2011). The case of E ($J-H$) $^{50}_{\mathrm{Xm}}$, used for the dark cloud survey in Dobashi (2011), is compared in this work (see the definition of E ($J-H$) $^{50}_{\mathrm{Xm}}$ described in Dobashi 2011). The LMC and SMC were masked because they did not derive the extinction of the LMC and SMC.

Figure 4.12 shows the results of the comparison between this work and Dobashi (2011). The A_V (2MASS) are saturated at A_V (2MASS) > 20 mag, indicating that the method of Dobashi (2011) has an upper limit of A_V (2MASS) = 20 mag. It is apparent that this method is not useful for $A_V > 20$ mag even though the upper limit of $A_V = 20$ mag is four times as large as that of the visual extinction derived by Dobashi et al. (2005). The visual extinction derived by Dobashi (2005) was saturated at $A_V = 5$ mag in the Cygnus region (Chapter 3). A_V (2MASS) is systematically smaller than A_V (case I) of 1 – 10 mag because galactic dust may exist behind the stars cataloged in the 2MASS PSC. A scatter that appears in the vertical direction at A_V (case I) < 1 mag is probably caused by the low S/N of A_V (2MASS) in high galactic latitudes. Dobashi (2011) employed a larger beam size in high latitudes than that in the galactic plane to achieve a constant noise level. The extinction in high latitudes was smaller than that in the galactic plane. The 1σ noise level is 0.4 mag in A_V (2MASS). The mean uncertainty of this work was 0.07 mag within $|b| > 45^\circ$.

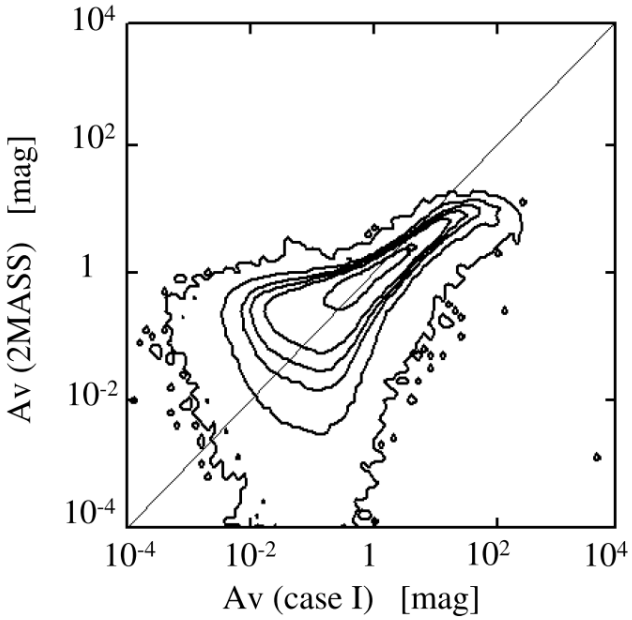

Figure 4.12: Comparison of A_V between this work and Dobashi (2011). The A_V (2MASS) are saturated at A_V (2MASS) > 20 mag. The scatter in the vertical direction at A_V (case I) < 1 mag may be caused by the low S/N of A_V (2MASS) in high galactic latitudes. The solid line indicates the slope of unity. LMC and SMC are masked. The contour map includes the same parameters as those described in Figure 4.7. The average number of data points contained in each bin is 732.

Figure 4.13 shows a histogram of A_V (2MASS) □ A_V (case I). The mean, median, and standard deviation of the A_V difference are □0.58, □0.09, 3.69 mag, respectively. Figure 4.14 shows the distributions of the A_V difference between this work and Dobashi (2011). A systematic difference is seen in the galactic plane. The mean and median within $|b| < 45^\circ$ are □0.75 and □0.10 mag, respectively. A scatter appears in high galactic latitudes. The standard deviation within $|b| > 45^\circ$ is 0.34 mag.

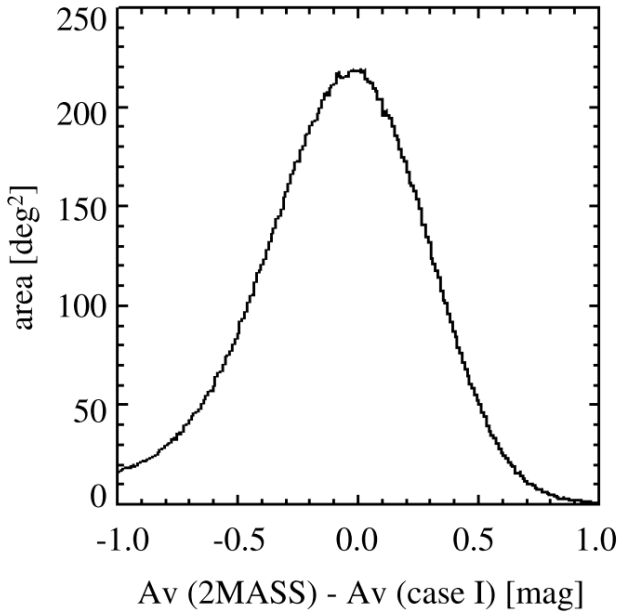

Figure 4.13: Histogram of the A_V difference between this work and Dobashi (2011). Bin size is 0.01 mag. The mean, median, and standard deviation of the A_V difference are −0.58, −0.09, 3.69 mag, respectively. LMC and SMC are masked.

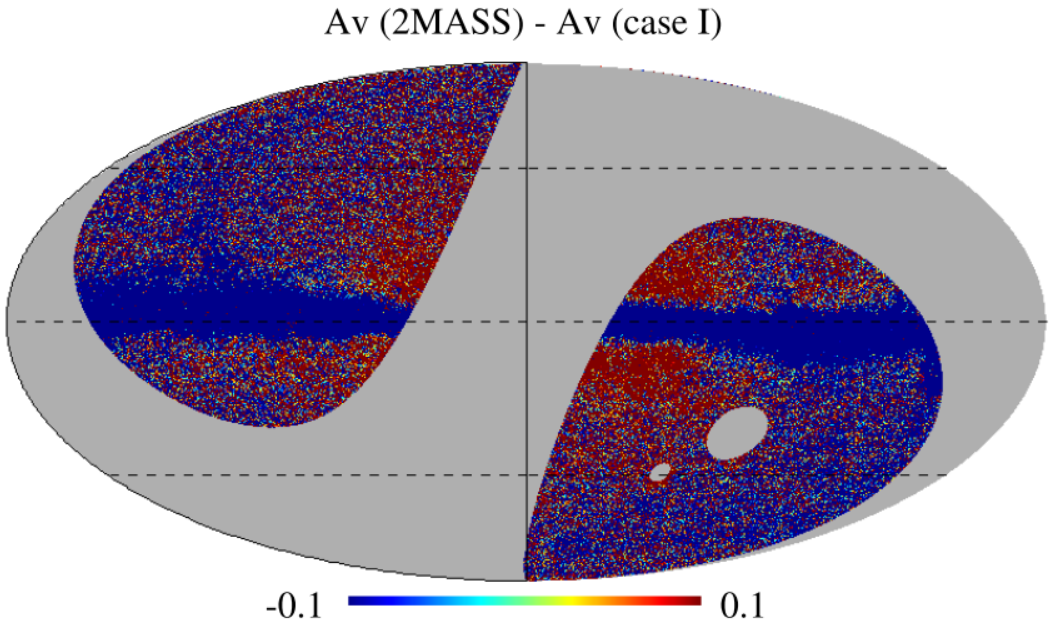

Figure 4.14: Map of the A_V difference between this work and Dobashi (2011). The range is ± 0.1 mag. LMC and SMC are masked.

Figure 4.15 shows the area in which the A_V difference between this work and Dobashi (2011) is larger than the A_V uncertainty of this work, as shown in the following equation:

$$\left|A_V(\mathrm{2MASS}) - A_V(\mathrm{case\,I})\right| > \Delta A_V . \qquad (4.3)$$

The area represented in Figure 4.15 occupies 81% of the region $|\beta| > 30^\circ$. The A_V (2MASS) and A_V (case I) are consistent in middle-galactic latitudes, which indicates that the near-infrared extinction above the middle-galactic latitudes may trace most of the dust column in the Galaxy along a line of sight. In the area represented in Figure 4.15, the extinction should be estimated by the method of this work rather than of Dobashi (2011)'s method with respect to estimation of the extragalactic reddening. However, the method of this work may not be suitable as an estimator of the reddening for objects located in the galaxy because the extinction derived in this work reflects the entire integration through the galaxy.

The area in which the significant difference is confirmed becomes larger if the author take case I or case II. If case I only is assumed, the area occupies 90% of the region with $|\beta| > 30^\circ$.

Dobashi (2011)'s overestimation of the extinction toward the galactic bulge (Figure 4.14) was probably because of uncertainty of the intrinsic star colors in the galactic bulge. The galactic bulge formation remains a topic for discussion (Robin et al. 2003). The overestimation also appears in a comparison between SFD and Dobashi (2011), wherein K. Dobashi also recognized their overestimation. In addition, he stated that A_V (2MASS) toward the galactic bulge should be considered with careful attention (private communication with Dobashi). A_V values derived by this work can be used of an upper limit for A_V (2MASS) toward the galactic bulge. A_V (SFD) within $|\beta| < 30^\circ$ is useful for the upper limit.

The A_V comparison results are summarized in Table 4.5.

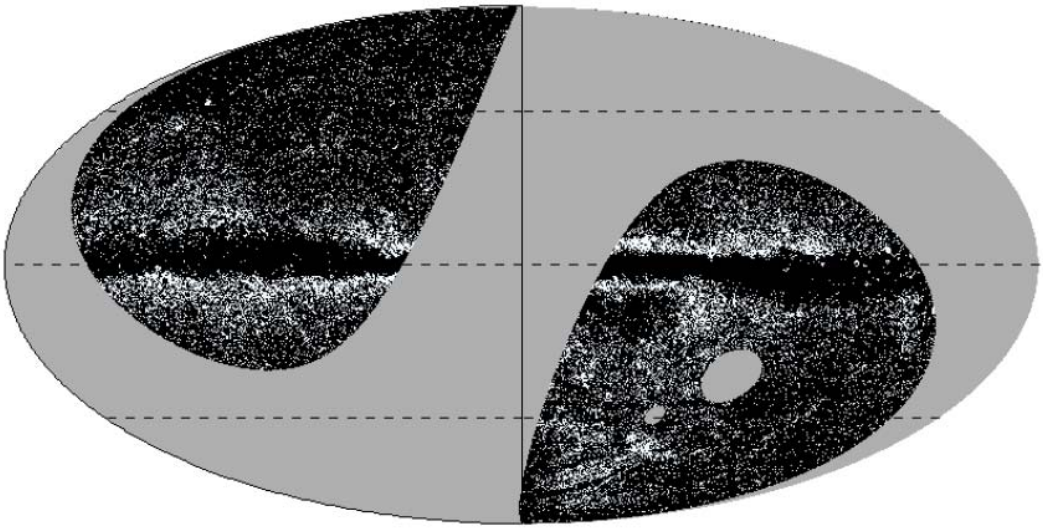

Figure 4.15: Area in which the significant difference between this work and Dobashi (2011) is confirmed. Black shading represents areas in which the difference is larger than the A_V uncertainty of this work. The area occupies 81% of the region with $|\beta| > 30^\circ$.

Table 4.5: Results of A_V comparisons between this work, SFD, and Dobashi (2011)

Method	Effective Region	Wavelength [μm]	Spatial resolution [arcmin]		1σ A_V difference between this work [mag]	Upper limit for A_V [mag]
			A_V	Dust temperature		
this work	$\|\beta\| > 30^\circ$	100 & 140	5	5	-	over 100
SFD	All-sky	100 & 240	5	42	2.29	over 100
Dobashi (2011)	All-sky	1.25 & 1.65	1-2	-	3.69	20

The A_V difference is compared with the result for case I; i.e., A_V (case I).

4.5 Summary

A new Galactic extinction map in high ecliptic latitudes with $|\beta| < 30^\circ$ were derived on the basis of far-infrared intensity and the dust temperature with a spatial resolution of 5′. The dust temperature was derived on the basis of intensities at 100 and 140 μm. The intensity at 140 μm was derived from the intensities at 60 and 100 μm of the *IRAS* data, assuming color-color correlations between the intensities at 60, 100, and 140 μm of the DIRBE data.

Two tight correlations in the region with $|\beta| > 30^\circ$ were identified. The DIRBE maps were spatially smoothed to increase the S/N of DIRBE140, particularly in high galactic latitudes. The two tight correlations showed separate relations depending on the antenna temperature of the radio continuum at 41 GHz.

The method of this work had a clear advantage over SFD because the spatial resolution of the dust temperature was 10 times higher than that of SFD. The accuracy was estimated to be as much as 5% and 21%, where A_V (SFD) is smaller and larger than 1 mag, respectively. A significant difference of A_V was confirmed in the comparison between this work and SFD. The area in which the deviation was larger than the A_V uncertainty of this work occupied 28% of the region with $|\beta| > 30^\circ$. In this area, the extinction should be estimated by the method of the present study rather than SFD's method.

The extinction map derived through this work was compared with that derived by Dobashi (2011). The A_V (2MASS) was saturated at $A_V > 20$ mag. A low S/N of A_V (2MASS) appeared in high galactic latitudes. The S/N of A_V (2MASS) was significantly smaller than that determined by this work. The area in which the significant difference was confirmed occupied 81% of the region with $|\beta| > 30^\circ$. In this area, the extinction should be represented by the method of the present study rather than Dobshi (2011)'s method with respect to the estimation of extragalactic reddening.

Chapter 5

Conclusion

The present study established a new method to derive the light extinction by the Galactic interstellar dust. In the present study the dust temperature distribution with a 5′ spatial resolution was derived. The 5′ resolution of the present study is 10 times higher than that of the standard method by Schlegel, Finkbeiner, & Davis (1998; SFD).

In the present study tight correlations between far-infrared intensities at 60, 100, & 140 μm were assumed. Hibi et al. (2006) found these correlations by the analysis of the DIRBE data in the galactic plane ($|b| < 5^\circ$). By assuming the correlations, the present study could derive the 140 μm intensity by the *IRAS* data at 60 & 100 μm with a 5′ spatial resolution. The dust temperature could be derived by the intensities at 140 & 100 μm. Maps of dust temperature and extinction were derived by the present method in the Cygnus region. Difference of spatial resolution between the present method and SFD was significantly larger than the uncertainty associated with derivation of the intensity at 140 μm in the present study.

Larger maps derived in a region with $|\beta| > 30^\circ$ on the basis of the method of the present study. Two correlations between the far-infrared intensities at 60, 100, & 140 μm were apparent. These correlations were divided by the radio continuum emission map at 41 GHz. An extinction map was derived assuming these correlations. A significant difference of A_V was confirmed in the comparison between this work and SFD. The area in which the deviation was larger than the A_V uncertainty of this work occupied 28% of the region with $|\beta| >$

30°. This area is concentrated in the galactic plane. It was because that the dust distribution in high galactic latitudes was more uniform than that in the galactic plane.

With respect to the estimation of extragalactic reddening, the extinction maps derived through this work were more accurate than the maps derived on the basis of star catalogs. A_V derived by this work has an upper limit at $A_V > 100$ mag. On the other hand, A_V of DSS (Dobashi et al. 2005) was saturated at $A_V > 5$ mag. A_V of 2MASS (Dobashi 2011) was saturated at $A_V > 20$ mag. The area in which the significant difference between this work and Dobashi (2011) was confirmed occupied 81% of the region with $|\beta| > 30°$.

Future prospects to derive a more accurate extinction map are described below.

Observation results of *AKARI*/FIS (Murakami et al. 2007; Kawada et al. 2007) should be compared with the results of this work. The Far-Infrared Surveyor (FIS) on the *AKARI* satellite observed the all-sky intensities at 65, 90, 140, and 160 μm with a spatial resolution of 1′. The FIS results are independent of the result of this work. The FIS observed data at 65 and 100 μm will be calibrated by the *IRAS* and DIRBE data. The FIS observation data at 140 μm can be calibrated by the DIRBE data. Therefore, with respect to the spatial resolution, the FIS calibration accuracy at 140 μm is 1°. The calibration accuracy of FIS is expected to increase by the comparison with this work. In addition, FIS could remove a point-source contamination that was indicated by Yahata et al. (2007) in the *IRAS* 100 μm intensity map.

The High Frequency Instrument (HFI) on the *Planck* satellite has observed the all-sky intensities at 350 μm to 3 mm (Planck HFI Core Team 2011a, b). Planck collaboration (2011) derived the dust temperature with a 4′ spatial resolution. *Planck*/HFI showed photometric bands at the Rayleigh-Jeans tail of dust emission with a 4′ spatial resolution. The spatial resolution was nearly equal to that of this work. Planck collaboration (2011) derived the dust temperature distribution on the basis of intensities at 100 and 350 μm. The *IRAS* data was used as the intensity at 100 μm in Planck collaboration (2011). Planck collaboration (2011) assumed the spectral emissivity index of $\beta = 1.8$. Some observational results show that β changes depending on the physical status of the ISM (e.g., Reach et al. 1995; del Burgo et al. 2003). If significant difference between *Planck*'s result and this work is confirmed, the validity of the spectral emissivity index of dust emission should be examined. The true spectral

emissivity index of dust is still an open question. Anti-correlation between the spectral emissivity index and dust temperature has been indicated (Dupac et al. 2003; Liang, Fixsen, & Gold 2012). On the other hand, Shetty et al. (2009) indicated that this anti-correlation could be caused by the noise of flux used in anti-correlation analysis.

References

Aannestad, P. A., Kenyon, S. J., 1979, ApJ, 230, 771

Abazajian, K. N., et al. 2009, ApJS, 182, 543

Arce, H. G., Goodman, A. A., 1999a, ApJ, 512, L135

Beichman, C. A., Neugebauer, G., Habing, H. J., Clegg, P. E., & Chester, T. J. (ed.) 1988, Infrared Astronomical Satellite (*IRAS*) Catalogs And Atlases, Vol. 1: Explanatory Supplement (Washington, DC: US Government Printing Office)

Bot, C., Helou, G., Boulanger, F., Lagache, G., & Miville-Deschênes, M.-A. 2009, ApJ, 695, 469

Burstein, D., & Heiles, C. 1978, ApJ, 225, 40

Burstein, D., & Heiles, C. 1982, AJ, 87, 1165

Cardelli, J. A., Clayton, G. C., & Mathis, J. S. 1989, ApJ, 345, 245

COBE Diffuse Infrared Background Experiment (DIRBE) Explanatory Supplement, version 2.3. 1998, ed. Hauser, M. G., Kelsall, T., D. Leisawitz, & Weiland, J. (Greenbelt, MD: NASA/GSFC), available from the NSSDC

del Burgo, C., Laureijs, R. J., Ábrahám, P., & Kiss, Cs. 2003, MNRAS, 346, 403

Désert, F.-X., Boulanger, F., & Puget, J. L. 1990, A&A, 237, 215

Dobashi, K., Uehara, H., Kandori, R., Sakurai, T., Kaiden, M., Umemoto, T., & Sato, F. 2005, PASJ, 57, 1

Dobashi, K., 2011, PASJ, 63, 1

Draine, B. T., & Anderson, N. 1985, ApJ, 292, 494

Draine, B. T., & Lee, H. M. 1984, ApJ, 285, 89

Draine, B. T., & Li, A. 2007, ApJ, 657, 810

Górski K. M., Hivon E., Banday A. J., Wandelt B. D., & Hansen, F. K., 2005, ApJ, 622, 759–771

Faber, S. M., Wegner, G., Burstein, D., Davies, R. L., Dressler, A., Lynden-Bell, D., & Terlevich, R. J. 1989, ApJS, 69, 763
Greenberg, J. M. 1968, in Stars and Stellar Systems, Vol. 7, ed. B. M. Middlehurst & L. H. Aller (Chicago: Univ. of Chicago Press), 221
Handa, T., Sofue, Y., Nakai, N., Hirabayashi, H., & Inoue, M. 1987, PASJ, 39, 709Hauser, M. G. et al. 1998, ApJ, 508, 25
Hibi, Y., Shibai, H., Ootsubo, T., & Hirashita, H. 2006, PASJ, 58, 509
Hirashita, H., Hibi, Y., & Shibai, H. 2007, MNRAS, 379, 974
Hirashita, Y. and Ichikawa, T., T., 2009, MNRAS, 396,500
Jarosik N. et al. 2011, ApJS, 192, 14
Kawada, M. et al. 2007, PASJ, 59, 389
Kelsall, T. et al. 1998, ApJ, 508, 44
Kohyama, T., Shibai, H., Fukagawa, M., & Hibi, Y. 2010, ApJ, 719, 873
Lada, C. J., Lada, E. A., Clemens, D. P., & Bally, J. 1994, ApJ, 429, 694
Lasker, B. M. 1994, BAAS, 26, 914
Li, A., & Draine, B. T. 2002, ApJ, 576, 762
Liang, Z, Fixsen, D. J., & Gold. B. 2012, arXiv:1201.0060v1
Mathis, J. S. 1990, ARA&A, 28, 37
Matsuura et al. 2011, ApJ, 737, 2
Miville-Deschênes, M.-A., Lagache, G., & Puget, J.-L. 2002, A&A, 393, 749
Miville-Deschênes, M.-A., & Lagache, G. 2005, ApJS, 157, 302
Murakami, H., et al. 2007, PASJ, 59, S369
Planck HFI Core Team. 2011a, Planck early results 04: First assessment of the High Frequency Instrument in-flight performance, arXiv1101.2039v1
Planck HFI Core Team. 2011b, Planck early results 06: The High Frequency Instrument data processing, arXiv1101.2048v1
Planck Collaboration. 2011, Planck early results 19: All-sky temperature and dust optical depth from Planck and IRAS — constraints on the “dark gas” in our Galaxy, arXiv1101.2029v1
Robin, A., C. et al. 2003, A&A, 409, 523
Reach, W. T. et al. 1995, ApJ, 451, 188
Rowles, J., & Froebrich, D. 2009, MNRAS, 395, 1640
Schlegel, D. J., Finkbeiner, D. P., & Davis, M. 1998, ApJ, 500, 525 (SFD)
Shetty, R., Kauffmann, J., Schnee, S., & Goodman, A. A. 2009, ApJ, 696, 676
Skrutskie et al. 2006, AJ, 131, Issue 2, 1163

Wheelock, S. L., et al. 1994, *IRAS* Sky Survey Atlas: Explanatory Supplement (Pasadena: JPL 94-11)

Whittet, D. C. B. 1992, Dust in the Galactic Environment (Bristol: IOP)

Wilkinson Microwave Anisotropy Probe (*WMAP*): Seven-Year Explanatory Supplement, editor M. Limon, et al. (Greenbelt, MD: NASA/GSFC)

Xilouris, E., Alton, P., Alikakos, J., Xilouris, K., Boumis, P., & Goudis, C. 2006, 651, L107

Yahata, K., Yonehara, A., Suto, Y., Turner E. L., Broadhurst, T., & Finkbeiner, D. P. 2007, PASJ, 59, 205

Yasuda, N., et al. 2001, ApJ, 122, 1104

York, D. G., et al. 2000, AJ, 120, 1579

Yun, M. S., Ho, P. T. P., & Lo, K. Y. 1994, Nature, 372, 530

Appendix A

Galaxy Number Count

Apparent magnitude in galaxy number counts must be corrected for the extinction. Galaxy number counts are represented by both the number density per solid angle and its flux. This must be due to both the actual number and bright, and so depend on the luminosity evolution of individual galaxies and number evolution of galaxies. Galaxy evolution can be discussed by comparing observed number counts with galaxy evolution models.

Luminosities of galaxies are assumed to be absolutely same. Intrinsic surface number density of galaxies, $S_{\mathrm{intrinsic}}$ [deg^{-2}], can be described by the following equation assuming a uniform distribution

$$S_{\mathrm{intrinsic}}(>F_{\mathrm{min}}) \propto F_{\nu}^{-1.5}, \tag{A.1}$$

where F_{ν} is flux density, and F_{min} shows flux limit. Galaxy distribution is actually not uniform. Equation (A.1) can be described by the following equation with a parameter α, which shows a galaxy distribution

$$S_{\mathrm{intrinsic}}(>F_{\mathrm{min}}) \propto F_{\nu}^{-\alpha} \tag{A.2}$$

Actually α is over 0 because the number density increases as the flux declines. Generally Equation (A.2) is represented with the apparent magnitudes, m_ν = constant – $2.5\log_{10}F_\nu$ as

$$S_{\text{intrinsic}}(< m_{\text{min}}) \propto 10^{0.4\alpha m_\nu}, \tag{A.3}$$

where m_{min} shows magnitude limit. Observed surface number density can be extinct with a certain degree of the extinction. Extinct surface number density at V band, $S_{\text{extinct,}}$ can be described as

$$S_{\text{extincted}} \propto 10^{0.4\alpha(m_V - A_V)}. \tag{A.4}$$

If the extinction is corrected by the A_V of SFD, this corrected surface number density, $S_{\text{corrected\_by\_Av (SFD)}}$, is described as the following equation:

$$S_{\text{corrected\_by\_}A_V\text{(SFD)}} \propto 10^{0.4\alpha(m_V - A_V + A_V\text{(SFD)})}. \tag{A.5}$$

If SFD estimate the extinction with no error, the intrinsic surface number density (Equation (A.3) is obtained. The difference between the true extinction and the extinction derived by SFD exists because of a poor spatial resolution of the dust temperature. This difference, ΔA_V, can be written by Equation (A.6) assuming the true extinction is estimated by this work;

$$S_{\text{corrected\_by\_}A_V\text{(SFD)}} \propto 10^{0.4\alpha(m_V + \Delta A_V)}, \tag{A.6}$$

where $\Delta A_V = A_V$ (SFD) – A_V (this work). This A_V difference can lead the difference of the surface number density as written by the following equation:

$$\frac{S_{\text{corrected\_by\_}A_V\text{(SFD)}}}{S_{\text{intrinsic}}} \propto 10^{0.4\alpha\,\Delta A_V}. \tag{A.7}$$

Equation (A.7) means that surface number density can be overestimated with SFD's extinction map in a region where $\Delta A_V > 0$ (i.e., where SFD overestimates the extinction). Schematic explanation is shown in Figure A.1. In the case $|\Delta A_V|$ of 0.1 mag, overestimation of 14% is expected assuming the uniform distribution (i.e., α = 1.5, Figure A.2). $|\Delta A_V|$ of 0.1 mag is confirmed in the comparison between this work and SFD (Figure 4.9). Galaxy number counts on the basis of the SDSS survey around V band detected a few hundred galaxies in a solid angle (e.g., Yasuda et al. 2001; Yahata et al. 2007). Extinction in the SDSS observations is usually corrected by SFD. A few dozen of galaxies in a line of sight can be overestimated if ΔA_V of 0.1 mag is exists there.

An observed surface number density in bright apparent magnitudes tends to

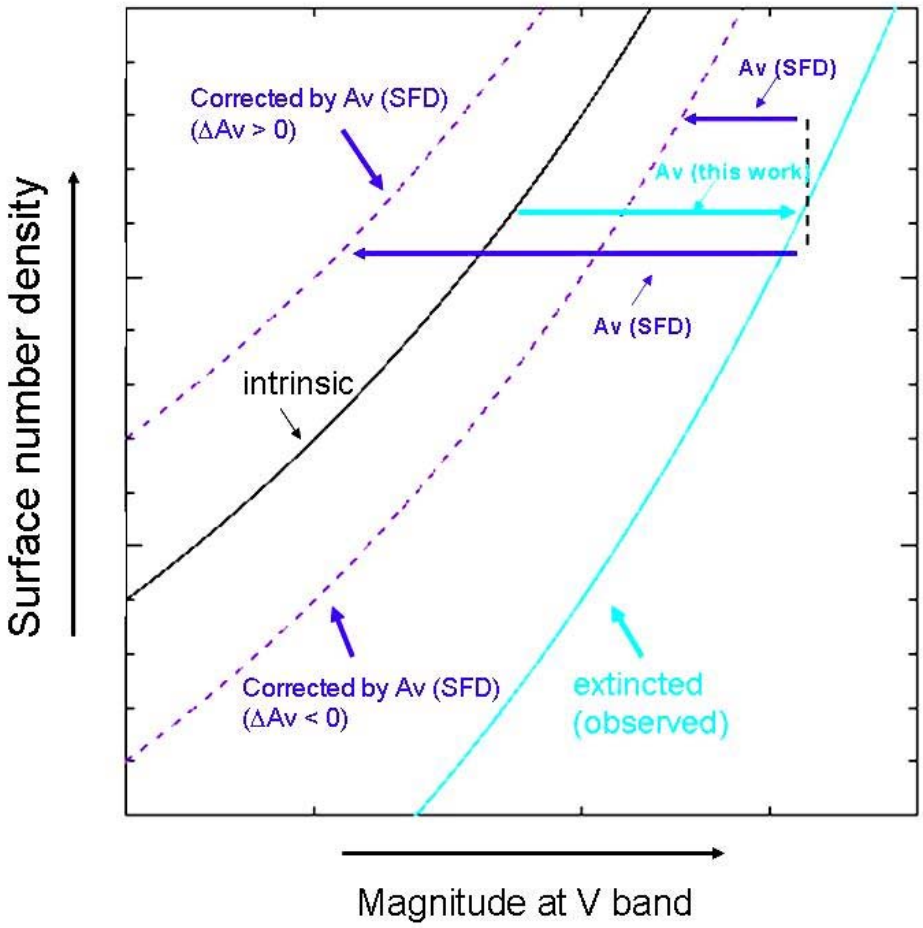

Figure A.1: Schematic explanation for the extinction correction for surface number density of galaxy under an assumption that the true extinction is estimated by this work. Each curve shows a surface number density depending on apparent magnitude at V band. Extinction is in the horizontal direction. ΔA_V means the difference between the true extinction and the extinction derived by SFD, and is defined as A_V (SFD) – A_V (this work). The difference of lengths between A_V (SFD) – A_V (this work) corresponds to ΔA_V.

be consistent with the uniform distribution model (i.e., α = 1.5). In the faint magnitudes, an observed surface number density tends to be consistent more moderate distribution of α = 1.0. For example, this α change is apparent in a surface number density derived by Yasuda et al. (2001) at r-band (0.63 μm), which is closed to V band. This change is apparent at m_r = 17 mag in Yasuda (2001). Surface number difference in the case of α = 1.0 is shown in Figure A.2. Overestimation of 9% is expected in the case of $|\Delta A_V|$ assuming α = 1.0.

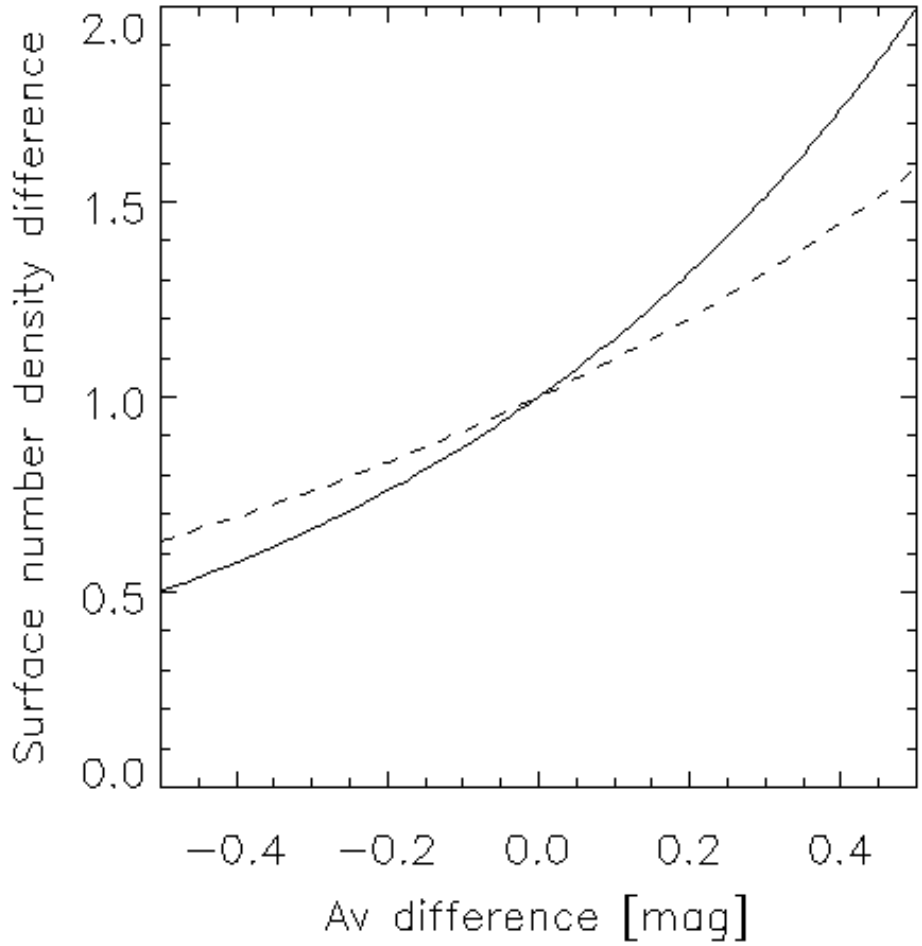

Figure A.2: Surface number density difference estimated by Equation (A.7). A_V difference (i.e., ΔA_V) is A_V (SFD) – A_V (this work). Solid and dashed curve show the case of α =1.5 (i.e., uniform distribution) and α = 1.0, respectively. The case of α = 1.0 is actually observed at the faint magnitudes (e.g., Yasuda et al. 2001)

Appendix B

A Galactic Extinction Map of the M81 & M82 Group

Neutral hydrogen gas is seen around the intergalactic space of the M 81 − M 82 group (Yun et al. 1994). The presence of dust between the group members is also revealed through systematic reddening of photometric color of background galaxies viewed through the intergalactic medium (Xilouris et al. 2006). Xilouris et al. (2006) examined the photometric color of background galaxies viewed through the intergalactic medium of the M81 group (Figure B.1). Any systematic reddening of the background objects, compared to the same population viewed adjacent to the group, reveals the presence of dust residing between the group members (galactic dust absorbs more blue than red light, thus both attenuating and reddening light from background sources). The dust-to-gas ratio is 10 times higher than that in the solar neighborhood.

Xilouris et al. (2006) corrected the Galactic extinction with the SFD's extinction map. Therefore the estimation of the systematic reddening of the background objects may have a certain degree error that is arisen from a poor spatial resolution of the dust temperature distribution. Figure B.2 shows the map of the A_V difference between this work and SFD. Av of This work is

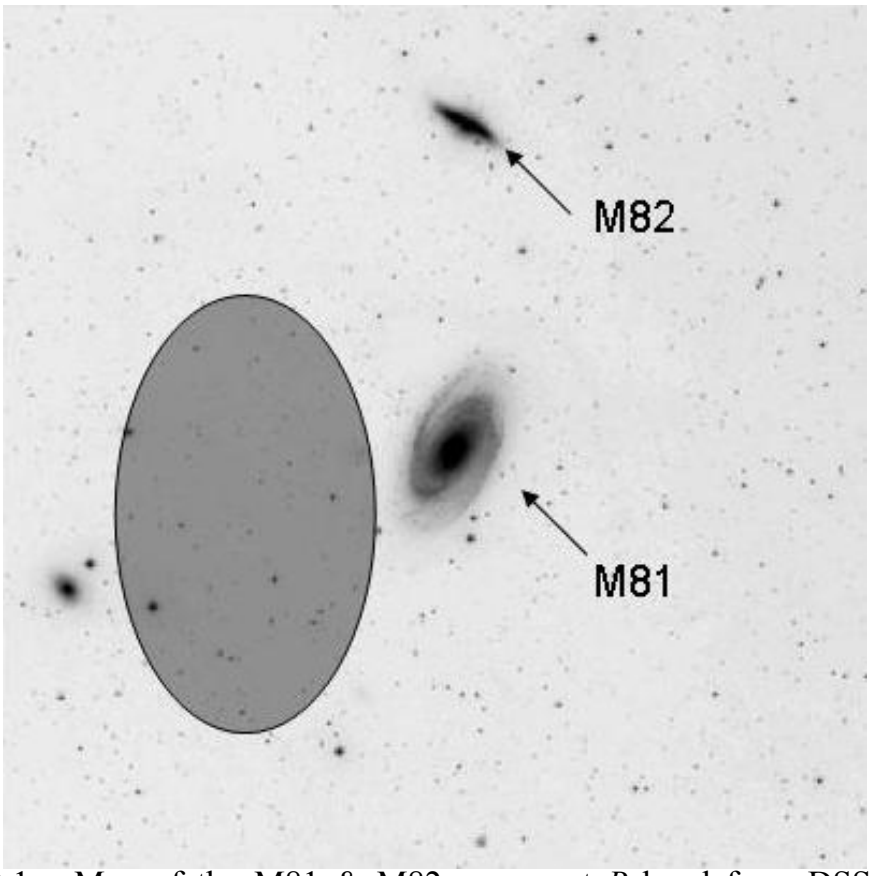

Figure B.1: Map of the M81 & M82 groups at *B* band from DSS (2˚×2˚). Black shading within a circle roughly represents area where the presence of the intergalactic dust is indicated by Xilouris et al. (2006).

represented by A_V (case I) that is derived in Chapter 4. A_V difference of A_V (SFD) – A_V (case I) is about ±0.2 mag where the intergalactic dust exists. This corresponds to E ($B-V$) difference of ±0.06 mag assuming R_V = 3.1. The presence of dust between the group members is still indicated even if the Galactic extinction estimation is decreased as much as ±0.06 mag in E ($B-V$). The presence of dust will not be indicated if the Galactic extinction estimation decreases as much as −0.10 mag in E ($B-V$).

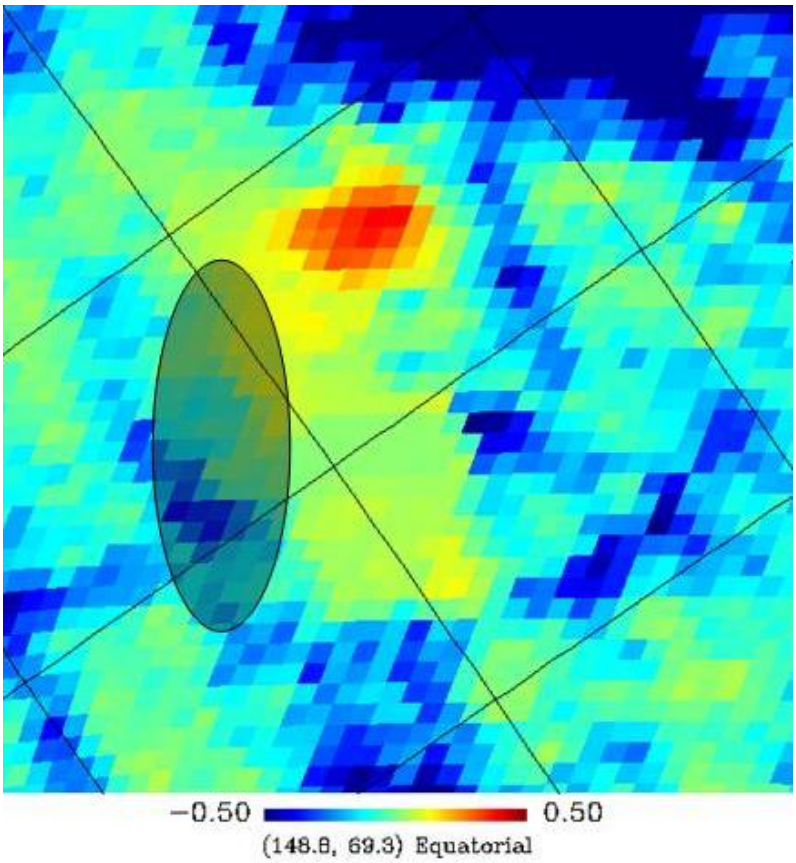

Figure B.2 Map of the A_V difference of A_V (SFD) − A_V (case I) in the M81 & M82 groups (2˚×2˚). Range is ± 0.5 mag. Black shading within a circle roughly represents area where the presence of the intergalactic dust is indicated by Xilouris et al. (2006). A_V difference within this circle is about ± 0.2 mag. Pixel scale is set to a 3′. 4 scale (Nside = 1024).

Appendix C

List of Publications

C.1 Referred Paper

1. Kohyama, T., Shibai, H., Fukagawa, M., & Hibi, Y. 2010, “A New Galactic Extinction Map of the Cygnus Region”, The Astrophysical Journal, 719, 873

2. Kohyama, T., Shibai, H., Kawada, M., Watabe, T., Matsuo, T., Mochizuki, S., Matsumoto, Y., Morishita, H, & Doi, Y. 2010 “Far-Infrared Interferometric Telescope Experiment (FITE): II. Sensor Optics”, Transactions of Space Technology Japan, 7, Tm_55

3. Nakashima, A., Shibai, H., Kawada, M., Matsuo, T., Narita, M., Kato, E., Kanoh, T., Kohyama, T., Matsumoto, Y., Morishita, H., Watabe, T., Yamamoto, K., Tanabe, M., Kanoh, R., & Itoh, Y. 2011, “Far-Infrared Interferometric Telescope Experiment (FITE): Three-Axis Stabilized Attitude Control System”, Transactions of the Japanese Society for Artificial Intelligence, Aerospace Technology Japan, 8, Tm_19

C.2 Award

Best Poster Award

Kohyama, T., Shibai, H., Mitsunobu, K., Watabe, T., Matsuo, T., Ohkubo, A., Katoh, E., Kanoh, T., Suzuki, M., Mochizuki, S., Matsumoto, Y., Morishita, H., Yamamoto, K., Kanoh, R., Nakashima, A., Tanabe, M., Doi, Y., Narita, M., 2008, "Far-Infrared Interferometric Telescope Experiment (FITE): Sensor Optics", Optical and Infrared Interferometry. Edited by Schöller, M., Danchi, W. C.; Delplancke, F. Proceedings of the SPIE, Volume 7013, pp. 70133O-70133O-10

C.3 Conference Proceedings

1. 幸山常仁、芝井 広、日比康詞、平下博之、深川美里、"A Galactic Extinction Map with High Resolution"、銀河のダスト研究会、2009 年 1 月、名古屋大学、Edited by Inoue, A., Takeuchi, T. T., Kaneda, H., & Hirashita, H.

2. Shibai, H., Fukagawa, M., Kato, E., Kanoh, T., Kohyama, T., Itoh, Y., Yamamoto, K., Kawada, M., Watabe, T., Nakashima, A., Tanabe, M., Kanoh, R., Narita, M. "Far-Infrared Interferometric Experiment (FITE): Toward the First Flight", Pathways Towards Habitable Planets, proceedings of a workshop held 14 to 18 September 2009 in Barcelona, Spain. Edited by Vincent Coudé du Foresto, Dawn M. G., & Ignasi R. San Francisco: Astronomical Society of the Pacific, p.541

3. Shibai, H., Fukagawa, M., Kato, E., Kanoh, T., Kohyama, T., Itoh, Y., Yamamoto, K., Shimoura, M., Kuwada, Y., Kawada, M., Watabe, T., Nakashima, A., Narita, M., Yoshida, T., Saito, Y., Matsuo, Y., Magalhaes M. A., Vilas-Boas W. J. "Far-Infrared Interferometric Telescope Experiment: FITE" Sixth Symposium on Extrasolar Planets, 18-20, Jan. 2010, Mitaka

4. Shibai, H., Matsuo, T., Kato, E., Kanoh, T., Kawada, M., Watabe, T., Kohyama, T., Matsumoto, Y., Morishita, H., Narita, M. “"FITE: Far-Infrared Interferometric Telescope Experiment"”, 27th International Symposium on Space Technology and Science, 2009-m-30, Tsukuba, 5-12, July 2009

5. Kanoh, T., Shibai, H., Fukagawa, M., Matsuo, T., Kato, E., Itoh, Y., Kawada, M., Watabe, T., Kohyama, T., Matsumoto, Y., Morishita, H., Yamamoto, K., Kanoh, R., Nakashima, A., Tanabe, M., Narita, M.,“Development of the Far-Infrared Interferometric Telescope Experiment”, Exoplanets and Disks: Their Formation and Diversity, The 2nd Subaru International Conference, Hawaii, 9-12 March 2009. p. 389

6. 叶 哲生、芝井 広、深川美里、加藤恵理、幸山常仁、伊藤優佑、山本広大、金子有紀、下浦美那、会見有香子、栄田嘉大、Dimitrios Kontopoulos、渡部豊喜、松尾太郎、川田光伸、成田正直 “遠赤外線干渉計 FITE のフライト計画”、大気球シンポジウム、JAXA/ISAS、9 月、2010、p. 96

7. 叶 哲生、芝井 広、松尾太郎、加藤恵理、伊藤優佑、川田光伸、幸山常仁、松本有加、森下祐乃、狩野良子、田辺光弘、中島亜紗美、山本広大、渡部豊喜、成田正直、土井靖生 “遠赤外線干渉計 FITE の地上試験と観測計画”、大気球シンポジウム、JAXA/ISAS、9 月、2008、p. 61

8. 望月 駿、芝井 広、川田光伸、渡部豊喜、松尾太郎、大久保篤史、加藤恵理、叶 哲生、鈴木未来、幸山常仁、松本有加、森下祐乃、狩野良子、土井靖生、藤原幹生、他 FITE チーム、”気球搭載遠赤外線干渉計用圧縮型 Ge:Ga 検出器アレイの開発”、 大気球シンポジウム、JAXA/ISAS、12 月、2007、p. 100

Appendix D

List of Presentations

D.1 Oral Presentation

1. 幸山常仁、芝井 広、深川美里、日比康詞、”高解像全天減光マップの作成 II”、日本天文学会秋季年会、鹿児島大学、9 月、2011、Q56a

2. 幸山常仁、芝井 広、深川美里、日比康詞、”高銀緯における銀河系ダストの遠赤外線放射の解析”、日本天文学会春季年会、広島大学、3 月、2010、Q37a

3. 幸山常仁、芝井 広、日比康詞、平下博之、深川美里、”高解像全天減光マップの作成”,日本天文学会春季年会、大阪府立大学、3 月、2009、Q36a

4. 幸山常仁、芝井 広、川田光伸、渡部豊喜、大坪貴文、松尾太郎、大久保篤史、加藤恵理、叶 哲生、鈴木未来、望月 駿、松本有加、森下祐乃、山本広大、狩野良子、田邊光弘、中島亜紗美、土井靖生、成田正直、”気球搭載遠赤外線干渉帰依 FITE: 極低温光学系の開発”、日本天文学会春季年会、国立オリンピック記念青少年総合センター、3 月、2008、W66a

5. 芝井 広、松尾太郎、加藤恵理、叶 哲生、伊藤優佑、川田光伸、渡部豊喜、幸山常仁、松本有加、森下祐乃、狩野良子、田邊光弘、中島亜紗美、山本広大、吉田哲也、斉藤芳隆、成田正直、Antonio, Mario, Magalhaes, Jose Williams Vilas-Boas “気球搭載遠赤外線干渉計 FITE：ファーストフライト準備”、日本天文学会春季年会、大阪府立大学、3 月、2009、W07a

6. 叶 哲生、芝井 広、松尾太郎、加藤恵理、伊藤優佑、川田光伸、渡部豊喜、幸山常仁、松本有加、森下祐乃、狩野良子、田邊光弘、中島亜紗美、山本広大、成田正直、“気球搭載遠赤外線干渉計 FITE：干渉光学系の性能評価”、日本天文学会春季年会、大阪府立大学、3 月、2009、W08a

7. 松本有加、渡部豊喜、芝井 広、松尾太郎、加藤恵理、叶 哲生、伊藤優佑、川田光伸、幸山常仁、森下祐乃、狩野良子、田邊光弘、中島亜紗美、山本広大、成田正直、“気球搭載遠赤外線干渉計 FITE：中間赤外線検出器”、日本天文学会春季年会、大阪府立大学、3 月、2009、W09a

8. 中島亜紗美、芝井 広、松尾太郎、加藤恵理、叶 哲生、伊藤優佑、川田光伸、渡部豊喜、幸山常仁、松本有加、森下祐乃、狩野良子、田邊光弘、山本広大、成田正直、“気球搭載遠赤外線干渉計 FITE：3 軸姿勢制御システム”、日本天文学会春季年会、大阪府立大学、3 月、2009、W09a

9. 加藤恵理、芝井 広、川田光伸、渡部豊喜、大坪貴文、松尾太郎、大久保篤史、叶 哲生、鈴木未来、望月 駿、幸山常仁、松本有加、森下祐乃、山本広大、狩野良子、田邊光弘、中島亜紗美、土井靖生、成田正直、”気球搭載遠赤外線干渉帰依 FITE: 干渉光学系”、日本天文学会春季年会、国立オリンピック記念青少年総合センター、3 月、2008、W63a

10. 叶 哲生、芝井 広、川田光伸、渡部豊喜、大坪貴文、松尾太郎、大久保篤史、加藤恵理、鈴木未来、望月 駿、幸山常仁、松本有加、森下祐乃、山本広大、狩野良子、田邊光弘、中島亜紗美、土井靖生、成田正直、”気球搭載遠赤外線干渉帰依 FITE: 光学系調整機構”、日本天文学会春季年会、国立オリンピック記念青少年総合センター、3 月、2008、W64a

11. 鈴木未来、芝井 広、川田光伸、渡部豊喜、大坪貴文、松尾太郎、大久保篤史、加藤恵理、叶 哲生、望月 駿、幸山常仁、松本有加、森下祐乃、山本広大、狩野良子、田邊光弘、中島亜紗美、土井靖生、成田正直、”気球搭載遠赤外線干渉帰依 FITE: 構造系”、日本天文学会春季年会、国立オリンピック記念青少年総合センター、3 月、2008、W65a

12. 森下祐乃、芝井 広、川田光伸、渡部豊喜、大坪貴文、松尾太郎、大久保篤史、加藤恵理、叶 哲生、鈴木未来、望月 駿、幸山常仁、松本有加、山本広大、狩野良子、田邊光弘、中島亜紗美、土井靖生、成田正直、”気球搭載遠赤外線干渉帰依 FITE: 構造系”、日本天文学会春季年会、国立オリンピック記念青少年総合センター、3 月、2008、W67a

D. 1.2 Poster Presentation

1. 幸山常仁、芝井 広、深川美里、日比康詞、”M81 方向の高解像減光の作成”、日本天文学会秋季年会、金沢大学、9 月、2010、Q28b

2. 芝井 広、深川美里、加藤恵理、叶 哲生、幸山常仁、伊藤優佑、下浦美那、金子有紀、栄田嘉大、川田光伸、渡部豊喜、中島亜紗美、山本広大、吉田哲也、斉藤芳隆、Antonio, Mario, Magalhaes, Jose Williams Vilas-Boas “気球搭載遠赤外線干渉計 FITE：初観測に向けて”、日本天文学会春季年会、広島大学、3 月、2010、W77b